

Analysis for satellite-based high-dimensional extended B92 and high-dimensional BB84 quantum key distribution

Arindam Dutta^{1,2,*}, Muskan^{1,†}, Subhashish Banerjee^{1,‡} and Anirban Pathak^{2,§}

¹*Department of Physics, Indian Institute of Technology Jodhpur, Jodhpur 342030, Rajasthan, India*

²*Department of Physics and Materials Science & Engineering,*

Jaypee Institute of Information Technology, A 10, Sector 62, Noida, UP-201309, India

A systematic analysis of the advantages and challenges associated with the satellite-based implementation of the high dimensional extended B92 (HD-Ext-B92) and high-dimensional BB84 (HD-BB84) protocol is analyzed. The method used earlier for obtaining the key rate for the HD-Ext-B92 is modified here and subsequently the variations of the key rate, probability distribution of key rate (PDR), and quantum bit error rate (QBER) with respect to dimension and noise parameter of a depolarizing channel is studied using the modified key rate equation. Further, the variations of average key rate (per pulse) with zenith angle and link length in different weather conditions in day and night considering extremely low noise for dimension $d = 32$ are investigated using elliptic beam approximation. The effectiveness of the HD-(extended) protocols used here in creating satellite-based quantum key distribution links (both up-link and down-link) is established by appropriately modeling the atmosphere and analyzing the variation of average key rates with the probability distribution of the transmittance (PDT). The analysis performed here has revealed that in higher dimensions, HD-BB84 outperforms HD-Ext-B92 in terms of both key rate and noise tolerance. However, HD-BB84 experiences a more pronounced saturation of QBER in high dimensions.

I. INTRODUCTION

In an information-centric society, safeguarding communications and data emerges as a fundamental necessity. This necessity spans various applications, including but not limited to financial transactions, upholding individual privacy, and preserving the integrity of vital components within the Internet of Things. Cutting-edge classical cryptosystems like Rivest-Shamir-Adleman (RSA) algorithm provide security that hinges on the computational complexity of a problem and associated assumptions about the computational power of the adversaries [1]. However, these assumptions can be compromised once large-scale quantum computers come into play [2]. The remedy for this challenge is provided by a relatively recent cryptographic concept known as quantum key distribution (QKD) [3–7]. Its security remains unaffected by algorithmic or computational progressions [8]. QKD enables the creation of symmetric keys between remote entities or parties, ensuring a level of confidentiality that is inherently constrained by the fundamental laws of physics [9, 10]. The polarization of light (photons) is a degree of freedom that is often utilized to realize different schemes for QKD and other schemes for secure quantum communication [11–21]. Drifting qubits encoded in photons have the potential to be distributed over a distance of at most a few hundred kilometers through optical fibers [22–25]. To extend these distances further, the utilization of quantum repeaters has been proposed [26, 27], but quantum repeaters are not yet commercially available. Further, maintaining light polarization possesses practical difficulties in long-distance QKD protocols. Improving the key rate and extending the range of QKD present a crucial challenge. This challenge, which may seem insurmountable without the implementation of quantum repeaters [27], revolves around surpassing the fundamental rate–distance limit inherent to QKD. This limit dictates the maximum secret key rate achievable between two parties over a given distance using QKD and is defined by the secret-key capacity of the quantum channel [28] linking these parties. In addition to the traditional QKD protocols, an alternative approach involves generating pairs of phase-randomized optical fields at separate distant locations, which are subsequently combined at a central measurement station. These fields, characterized by identical random phases, are termed as ‘twins’ and can be utilized to distill a quantum key. The key rate of this twin-field QKD follows a similar distance-dependent trend as a quantum repeater, scaling proportionally to the square root of the channel transmittance [29, 30]. However, compensating for channel fluctuations and locking laser fluctuations necessitates the use of phase tracking and phase locking techniques in experimental setups, significantly increasing complexity and impeding free-space implementation. Further advancements include the development of an asynchronous measurement-device-independent quantum key distribution protocol capable of surpassing secret key capacity even in the absence of phase tracking and

* arindamsalt@gmail.com; <https://orcid.org/0000-0003-3909-7519>

† muskan.1@iitj.ac.in; <https://orcid.org/0009-0009-1630-8898>

‡ subhashish@iitj.ac.in; <https://orcid.org/0000-0002-7739-4680>

§ anirban.pathak@gmail.com; <https://orcid.org/0000-0003-4195-2588>

phase locking [31–33]. While these schemes have been experimentally demonstrated to be effective under conditions of significant quantum channel attenuation [34–37], they hold promise for future applications in space-ground quantum key distribution.

In the case of QKD protocols based on optical fiber, the polarization state is susceptible to alterations caused by random fluctuations of birefringence in the optical fiber [38, 39]. Further, the diminishing signal strength and the interference from ambient noise experienced during QKD transmissions via optical fibers hinder the attainment of substantial key rates beyond networks of metropolitan proportions [40–42]. An alternative solution involves the proper utilization of optical satellite links, which can potentially overcome the limitations on transmission distances encountered by ground-based photonic communication schemes [43–45]. When dealing with open space conditions, while polarization exhibits greater resilience against atmospheric turbulence, in the reference frame of the satellite, variation of polarization is observed due to the motion of the satellite. This introduces a negative impact [46–48], and it becomes crucial to address these polarization fluctuations issues in both free-space and fiber-based QKD systems [49, 50]. Traditional approaches for addressing this challenge encompass the utilization of active polarization tracking devices [40, 51–55]. An alternative approach through a proof-of-principle experiment was proposed in 2023 [56]. Here, quantum state tomography was used to determine the optimal measurement bases for a single party. Moreover, embedding quantum technology within space platforms offers an avenue for conducting fundamental experiments in physics [57, 58] and pioneering innovative concepts like quantum clock synchronization [59–61] and quantum metrology [62]. Although this endeavor presents significant technological challenges, a variety of experimental investigations [63–70] alongside theoretical inquiries [44, 71] have showcased the feasibility of this approach. These studies have demonstrated the viability of this approach using state-of-the-art technology already in use on the ground and approved for space operations [72, 73]. In fact, over the last decade, numerous experiments in free-space conditions have been conducted to assess the practicality of QKD setups on mobile platforms, encompassing diverse vehicles like hot-air balloons [67], trucks [74], aircraft [68, 70], and drones [75]. Consequently, in what has been characterized as the *quantum space race* [76], multiple international research groups in countries like Canada, Japan, Singapore, Europe, and China have been actively participating and trying to establish stable space-based communication channels [41, 77]. Notably, these efforts have seen the successful launch of satellites with payloads capable of being used in quantum communication [78–84]. Furthermore, the development of a quantum internet is poised to be pivotal in introducing fundamentally novel internet technology, facilitating quantum communication between any two locations on Earth. This quantum internet, in conjunction with the existing “classical” internet infrastructure, will interlink quantum information processors, enabling the realization of capabilities that are demonstrably unattainable solely through classical information methods [85]. Through this quantum technology, the security objectives, specifically confidentiality, integrity, authenticity, and non-repudiation—will underpin diverse e-commerce transactions and the communication of sensitive information [86, 87]. The advancement of quantum technology has been greatly influenced by the healthy competition among the researchers [88–90], driving notable progress in quantum nonlinear optics, entangled photon generation techniques, and single photon detection in recent years. Given these remarkable technological strides, it is imperative to reevaluate the enhanced performance aspects of QKD through typical free-space connections. This reevaluation particularly focuses on the considerable rise in secure key generation rates compared to earlier experiments [63, 91–94] (see Figure 1 of Ref. [95]). While this analysis (refer to Figure 1 of Ref. [95]) does not incorporate field tests utilizing prepare-and-measure schemes, it is worth noting that both terrestrial [96, 97] and satellite-based [79, 98] studies have effectively demonstrated decoy-state key exchange across free-space links at high rates. Furthermore, entanglement-based QKD protocols eliminate the necessity to place trust in the source of the satellite in a dual down-link scenario. Motivated by these facts, in the present work we wish to investigate the effectiveness of two specific protocols for QKD for the long-distance free-space secure quantum communication to be implemented with the assistance of a satellite. Before we specifically mention the protocols selected here for the investigation, we would like to briefly mention the logical evolution of the relevant protocols that led to the protocols of our interest.

The first protocol for QKD was proposed by Bennett and Brassard in 1984 (BB84 protocol) [3]. From the introduction of the BB84 protocol, there has been a continuous progression in both theoretical and practical aspects of QKD [25, 99, 100]. Nonetheless, owing to the formidable challenges posed by the generation, maintenance, and manipulation of quantum resources using current technologies, there has been a concerted effort to formulate QKD protocols with more straightforward conceptual frameworks such that the protocols would require fewer quantum resources. For instance, the BB84 protocol itself involves four quantum states and two measurement bases. In 1992, Bennett introduced a notably simpler QKD protocol named B92, which relies solely on two non-orthogonal states and two measurement bases [5]. However, B92 exhibits a heightened susceptibility to noise in contrast to alternative protocols like BB84, as indicated in the original paper [5]. Subsequently, in 2009, Lucamarini et al. [101] introduced an extended version of B92 (Ext-B92), incorporating two extra non-informative states to more effectively constrain Eve’s information gain. BB84, B92, and Ext-B92 protocols and most of the other existing protocols for QKD utilize qubits, which are two-dimensional systems, as the means of communication between Alice and Bob. Nevertheless,

there have been limited investigations concerning the susceptibility of qudit-based schemes (i.e., schemes utilizing key encoding on d -level systems) to eavesdropping in the case of high dimensional systems. Initiatives are currently underway to establish and investigate qudit systems within laboratory settings [102, 103]. Quantum systems with dimensions higher than two have demonstrated numerous benefits and intriguing characteristics compared to protocols based on qubits (as briefly discussed in [104]). There have been several studies related to their continuous variable counterparts ([105] and references therein). Further, certain protocols have exhibited the ability to tolerate high levels of channel noise as the system dimension expands, as evidenced by various studies [106–109]. Motivated by these facts, in this article, we assess the performance of the key rate under different scenarios for the HD-Ext-B92 and HD-BB84 protocols. We calculate the key rate of the HD-Ext-B92 scheme without the inclusion of extra independent variables, in contrast to the method outlined in Ref. [110], which is explained further in Appendix A. We utilize the channel transmission η to evaluate our results, focusing on light propagation through atmospheric links using the elliptic-beam approximation originally presented by Vasylyev et al. [111, 112]. Additionally, we incorporate the generalized approach and varying weather conditions introduced in [113]. Specifically, we investigate the applications of these models in quantum communication using *Low Earth Orbit* (LEO) satellites. Here, it may be noted that the methodology proposed in [111–113] has a notable impact on the transmittance value, which is influenced by beam parameters and the diameter of the receiving aperture.

Before delving into our main text, it is important to state that a satellite-based link is of two distinct types: the up-link and the down-link. These links should not be considered symmetrical due to the crucial distinction in the order of signal beam traversal through the atmosphere and space. In the up-link scenario, the signal beam first encounters the atmosphere, where it is subject to the effects of turbulence and scattering particles. It then proceeds into the expanse of space over long distances, where beam broadening becomes the dominant factor affecting its characteristics. Conversely, in the down-link scenario, the beam travels through space first and then through the atmosphere. In this scenario, the primary factor influencing the signal beam’s journey through extended space is the pointing error. This contrast in the order of traversal results in unique requirements for the receiving equipment on the ground and in space [113, 114].

The remainder of this paper is structured as follows. Section II provides a detailed exploration of the HD-Ext-B92 and HD-BB84 protocols, alongside an extensive analysis of how atmospheric conditions affect satellite communication links and the elliptical approximation of beam deformation at the receiver. We also investigate the key rate and QBER under varying noise parameters to determine the noise tolerance of these higher-dimensional protocols. Section III presents a thorough evaluation of the performance of these high-dimensional protocols, supported by illustrative results from simulations. Finally, we summarize our paper with the findings being consolidated and deliberated upon in Section IV. Appendix A contains detailed calculations for deriving the key rate of the HD-Ext-B92 protocol, while Appendix B covers the first and second moments of the beam parameters for both the up-link and down-link, crucial for our simulation results.

II. PRELIMINARIES: HIGH-DIMENSIONAL B92 AND BB84 PROTOCOLS AND ELLIPTIC BEAM APPROXIMATION

Numerous researchers have extensively investigated the unconditional security of QKD-based protocols, and their research, (see for examples, [115, 116]) has consistently revealed increasingly robust results. For instance, in [116], a noise tolerance of 6.5% was reported for the B92 protocol. Depending on the user’s selected key encoding states, the noise tolerance for this B92 protocol can extend up to 11% in the asymptotic scenario, as demonstrated in [101]. This level of noise tolerance is comparable to that of BB84. In scenarios with a finite key length, as indicated in [117], the protocol still maintains a minimum noise tolerance of 7%. In this context, we summarize the key-rate analysis for HD-Ext-B92 and HD-BB84 protocols. We modify the calculation for HD-Ext-B92 using a theorem to eliminate any additional free parameters (as detailed in Appendix A). Additionally, we briefly delve into the methodology of elliptical beam approximation, designed to encompass satellite-based connections while accounting for signal losses in various real-world scenarios, including diverse weather conditions. This methodology is particularly tailored for application in LEO satellite contexts.

A. High-dimensional extended B92 protocol and high-dimensional BB84 protocol

Before going into the intricacies of higher-dimensional protocols, let’s briefly discuss the higher-dimensional quantum states utilized in performing HD-QKD schemes [104, 118]. Traditional two-level quantum systems, represented by discrete variable states [119–121], and continuous variable states [122–124] within a single degree of freedom (such as polarization), have historically been employed for communicating information as qubits. However, there is a growing

interest in exploring quantum information within larger Hilbert spaces, achieved either by increasing the number of qubits or by utilizing d-level quantum systems, known as qudits. The decision to expand into higher dimensions depends on the specific objectives of the task at hand. The overarching aim is to enhance the available dimensions to transmit more than one bit per photon from one party (Alice) to another (Bob). Various photonic degrees of freedom, such as orbital angular momentum [125], temporal mode [126], frequency mode [127], and spatial mode [128, 129], inherent to single photons, are natural candidates for realizing high-dimensional systems. However, implementing HD-QKD protocols ideally necessitates a reliable single-photon on demand source. While significant experimental efforts have been directed towards constructing such sources (see [130, 131] and references therein), weak coherent pulses (WCPs) generated by attenuating laser outputs are commonly used as an approximate single-photon source in many commercial products. The quantum state of a WCP resulting from laser attenuation can be characterized as follows:

$$|\alpha\rangle = |\sqrt{\mu}\exp(i\theta)\rangle = \sum_{k=0}^{\infty} \left(\frac{e^{-\mu}\mu^k}{k!} \right)^{\frac{1}{2}} \exp(ik\theta) |k\rangle,$$

here, the symbol $|k\rangle$ denotes a Fock state (k photon state) and the mean photon number is denoted as $\mu = |\alpha|^2 \ll 1$. Essentially, Alice generates a quantum state that can be conceptualized as a superposition of Fock states, characterized by a Poissonian photon number distribution expressed as $p(k, \mu) = \frac{e^{-\mu}\mu^k}{k!}$. When utilizing the WCP source for signal state generation, users encounter a probability of multi-photon pulses within the signal state. In this scenario, Eve may execute a photon number splitting (PNS) attack. Eve initiates the attack by employing a quantum non-demolition measurement (QND) to determine the photon number, subsequently obstructing the single-photon pulses and retaining one photon from the multi-photon pulses. To counter the threat of PNS attacks, the decoy state method is implemented [132, 133]. Notably, different intensities are employed for generating the signal particles and the decoy state, resulting in distinct photon number distributions. The security procedure involves intentional and random replacement of signal pulses with multi-photon pulses (decoy pulses) by legitimate users. Subsequently, they assess the loss of the decoy pulses. If the loss of decoy pulses is anomalously lower than that of signal pulses, the entire protocol is aborted. Conversely, if the decoy pulse loss aligns with certain expectations, the protocol continues. The estimation of signal multi-photon pulse loss is then conducted based on the decoy pulse loss, assuming similar values for the two losses. Within HD-QKD protocols, the decoy state serves as a crucial tool for scrutinizing potential eavesdropping activities and ensuring channel security.

1. HD-Ext-B92

Here, we summarize the HD-Ext-B92 protocol and recap some important steps involved in the *parameter estimation* process proposed in Ref. [110]. In fact, in this section, after briefly discussing the HD-Ext-B92 protocol we modify the derivation of the asymptotic key rate given in [110] (see Appendix A). It is apt to note that *negotiation efficiency* stands as a crucial parameter in determining the security and accuracy of the final cryptographic key [134–139]. This parameter encompasses several procedural steps, including quantum state preparation-measurement, data reconciliation, QBER estimation, parameter estimation, error correction, and privacy amplification¹. Before explaining the protocol, we would like to introduce the notations used and the methodology for achieving key rate. $|m\rangle$ and $|n\rangle$ are the fixed d-dimensional states and defined from d-dimensional computational basis states $\{|1\rangle, \dots, |m\rangle, |n\rangle, \dots, |d\rangle\}$, and $|\psi\rangle = \frac{1}{\sqrt{2}}(|m\rangle + |n\rangle)$ is a fixed state which is chosen from d-dimensional diagonal basis (X -basis) states. As previously elucidated, a photon can manifest as a high-dimensional system through the utilization of different photonic degrees of freedom. It is pertinent to mention that $|m\rangle$ and $|n\rangle$ denote specific higher-dimensional systems that signify distinct states within the photonic degrees of freedom. These states can be precisely measured by Bob using d-dimensional computational basis states. In the context of the HD-Ext-B92 protocol, Alice is only required to transmit three high-dimensional states. Simultaneously, Bob's task entails conducting either a computational basis measurement or a partial basis measurement in an alternative basis (POVM X). It is noteworthy that this partial measurement need only discriminate a specific superposition state as defined in the protocol and is not obliged to discern all the possible states (d states).

State preparation and transmission: Alice randomly chooses key-round and test-round. The key-round is employed for generating raw key bit and test-round is employed to estimate error for this protocol that will help to improve

¹ For simplicity, while evaluating the performance of the satellite-based HD-Ext-B92 and HD-BB84 protocols, we are intentionally excluding the incorporation of error correction and privacy amplification measures.

the negotiation efficiency. Alice generates a sequence using states $|m\rangle$ and $|\psi\rangle$ to represent classical bit values 0 and 1 during the key-round, respectively. To assess channel noise and security, she randomly includes decoy states in the sequence². Subsequently, Alice transmits the enlarged sequence to Bob while maintaining confidentiality of the basis information. During test-round, she uniformly prepares states $|m\rangle$, $|n\rangle$, or $|\psi\rangle$ with a random selection, inserts decoy states, and transmits the sequence to Bob. The basis information remains confidential until Bob performs measurements on the sequence.

Estimation of channel noise and loss: Alice communicates the position and basis information of the decoy state to Bob through a public classical announcement. Bob performs measurements on the decoy state and publicly discloses the obtained results. The comparison of these results allows for the calculation of channel noise. If the noise falls within the predetermined threshold, the protocol advances to the next step; otherwise, the protocol is aborted. The measurement of decoy states also serves to assess channel loss. In both the key round and the test round, the loss of signal particles corresponds to the loss occurring for the decoy state. This ensures the security of the channel against PNS attack.

Measurement and classical announcement: Following the security check conducted using the decoy state, Bob will proceed to measure each state within the received sequence. This measurement involves the elimination of decoy states, accomplished either using the Z basis or by a POVM bases defined by $\{|\psi\rangle\langle\psi|, I - |\psi\rangle\langle\psi|\}$, and referred to as POVM X . Here, the symbol I represents the d -dimensional identity operator. Bob sets the bit value as 1 when he observes $I - |m\rangle\langle m|$ by using measurement basis Z , i.e., any measurement outcome in Z basis other than $|m\rangle\langle m|$ ³; and he sets bit value 0 when his measurement outcome using POVM X is other than $|\psi\rangle\langle\psi|$. All other results are not taken into account as conclusive measurements. Alice and Bob discard the iteration for inconclusive outcomes in key-round, and determine the channel error rate in test-round by announcing their basis choices and measurement results using an authenticated classical channel. To enhance negotiation efficiency, we conduct parameter estimation and QBER analysis, taking into account a depolarizing channel with the consideration of the noise parameter q . In instances where a round is inconclusive or does not qualify as a key round, the obtained results are employed for parameter estimation. Finally, they run the error correction and privacy amplification protocols to get the final secure key. Here are some crucial formulations pertaining to parameter estimation, which contribute to deriving the key rate equation of the HD-Ext-B92 protocol. Depolarizing noise is a very general noise of the Pauli class of noise channels and can be obtained by twirling them in two dimensional quantum state. Any quantum channel can be twirled by the depolarizing channel. Our aspiration to expand randomized benchmarking to d -dimensions led to the selection of the depolarizing channel in the protocol.

$$\mathcal{D}_q(\rho) = \left(1 - \frac{d}{d-1}q\right)\rho + \frac{q}{d-1}I.$$

The observable statistics can be expressed within the context of a depolarizing channel scenario.

$$\begin{aligned} p_{mm} &= p_{nn} = p_{\psi\psi} = 1 - q, \\ p_{mc} &= p_{nc} = p_{\psi c} = \frac{q}{d-1}, \\ p_{m\psi} &= p_{n\psi} = p_{\psi m} = p_{\psi n} = \frac{1}{2} \left(1 - \frac{qd}{d-1}\right) + \frac{q}{d-1}. \end{aligned}$$

Supposing p_{ij} represents the joint probability associated with Alice's and Bob's raw bits being i and j , considering the scenario without eliminating that specific iteration. The values of observable probabilities under the simulated channel for parameter estimation are,

$$\begin{aligned} p_{00} &= \frac{1}{2M} (1 - p_{m\psi}), \\ p_{01} &= \frac{1}{2M} (1 - p_{mm}), \\ p_{10} &= \frac{1}{2M} (1 - p_{\psi\psi}), \\ p_{11} &= \frac{1}{2M} (1 - p_{\psi i}). \end{aligned}$$

In [110], authors proposed a collective attack by Eve in which she can independently and identically attack each round of the protocol. Eve also can delay measurement on her register (quantum memory) after completion of the protocol. The Devetak Winter key rate equation [140, 141] is used to compute the key rate in the asymptotic limit⁴:

² The decoy state is not required to be a higher-dimensional state; it can be a two-dimensional quantum state, qubit.

³ This process resembles the B92 protocol [5]. Alice utilizes the $|0\rangle$ and $|+\rangle$ states to encode 0 and 1, respectively. Bob deciphers 0 and 1 based on his measurement outcomes, which correspond to the $|-\rangle$ and $|1\rangle$ states, respectively.

⁴ For instance, we are interested in seeing the performance of satellite-based communication in the infinitely generated raw key scenarios.

$$R(a, b, E) = \lim_{N \rightarrow \infty} \frac{l}{N} = \inf [S(a|E) - H(a|b)], \quad (1)$$

this analysis helps us to obtain the minimum value of the key rate by subtracting conditional Shannon entropy $H(a|b)$ from conditional von Neumann $S(a|E)$. Here, $S(a|E)$ is defined as the entropy or the uncertainty present in Alice's classical register a given Eve's quantum memory E and $H(a|b)$ denotes the entropy present in Alice's register a given Bob's classical register b . Here, l is determined as a number of secret key bits over the transmission of N number of raw key. In Eq. (1), R elucidates the infimum value of key rate under all collective attacks performed by Eve. We apply *Theorem* [110, 142] introduced by Krawec and analyze the parameter estimation to derive $S(a|E)$ and $H(a|b)$, consequently enhancing negotiation efficiency, thereby contributing to the overall improvement of the security and correctness of the final key. This formulation also facilitates the determination of QBER for the HD-Ext-B92 protocol. Using these findings, we can establish the minimum value for the key rate by employing Equations (18) and (19) from Appendix A in Equation (1).

2. HD-BB84

In a two-level system, BB84 [3] protocol is well studied both in theoretical and experimental domains. Essentially two-dimensional quantum states (qubits) are used to realize this scheme for QKD which uses two mutually unbiased bases randomly. In a more general scenario, higher dimensional quantum systems (qudits) can be used to realize the same task (i.e., QKD), and such a modified version of BB84 protocol is referred to as *qudit-* (i.e., a quantum state in d -dimensional Hilbert space) based BB84 protocol or HD-BB84 protocol. Here, we briefly discuss the HD-BB84 protocol [143] and the necessary formulae to compute the secret key rate.

In this protocol, Bob generates a sequence of qudits, where each qudit represents a higher-dimensional quantum state. These states are prepared based on a randomly selected basis, chosen from two mutually complementary bases: $Z = \{|0\rangle, |1\rangle, \dots, |D-1\rangle\}$ and $X = \{|x_0\rangle, |x_1\rangle, \dots, |x_{D-1}\rangle\}$. The qudit sequence is generated using a WCP source, with the possibility of a PNS attack. To counter the threat of a PNS attack, Bob strategically introduces decoy states at random positions within the qudit sequence, expanding it. Upon receiving the enlarged sequence, Bob communicates the positions and basis information of the decoy states to Alice. Subsequently, Alice performs measurements on the decoy states and publicly announces the measurement outcomes. Both parties then compute the losses and errors incurred during the communication channel. If the error rate falls within the acceptable threshold, the protocol advances to the next stage. After discarding the decoy particles from the enlarged sequence, Alice proceeds with a measurement operation on the qudits. The measurement is performed by randomly selecting one of the two d -dimensional bases, namely Z and X . This process ensures the security and reliability of the quantum communication protocol, especially in the presence of potential PNS attacks. Subsequently, they announce their bases choice in a public authenticated classical channel [143]) and obtain correlated d -ary random variables when they use the same bases. With $\frac{1}{2}$ probability, Alice and Bob use different bases and yield uncorrelated results which are considered as discarded data after key-sifting sub-protocol. It is crucial to emphasize that the loss should be consistent for both decoy states and signal states, thereby ensuring the security of the channel. This method ensures that any effort made by an eavesdropper, Eve (who is unaware of the chosen basis), to obtain information about Bob's state will result in an error in transmission, which can subsequently be detected by the legitimate parties.

To ensure a smooth comprehension of readers we would like to provide a concise overview of key points discussed in Ref. [144]. In Ref. [144], authors have modified the Maassen and Uffink bound [145, 146] to establish a new bound on the uncertainties associated with the measurement results, contingent on the amount of entanglement between the measured particle (A), and the quantum memory (B). This relationship can be expressed mathematically as,

$$S(Z|B) + S(X|B) \geq \log_2 \frac{1}{C} + S(A|B), \quad (2)$$

where, Z and X are two possible observable like measurement bases and A refers to the qudit measured by Alice which is sent by Bob and B refers to the qudit which represents the quantum memory of Bob. S represents von Neumann entropy and $S(A|B)$ quantifies the amount of entanglement between A and B . $C := \max_{i,j} |\langle \phi_i | \psi_j \rangle|^2$, where $|\phi_i\rangle$ and $|\psi_j\rangle$ are the eigenvectors of Z and X , respectively. Using a result established by Devetak and Winter [140], the minimum limit on the quantity of key that Alice and Bob can extract from each state can be expressed as $S(Z|E) - S(Z|B)$ ⁵. This limit is applied when the eavesdropper is trying to obtain the key from the composite

⁵ Here, Z and X can be employed in a similar manner or with a similar effect.

quantum system⁶ ρ_{ABE} , where A is Alice's particle, B is Bob's quantum memory, and E is Eve's ancillary state. Equation (2) may be reformulated as $S(Z|E) + S(X|B) \geq \log_2 \frac{1}{C}$ (see Supplementary Information of [144]), and the key rate equation may be written as,

$$\begin{aligned} r(A, B, E) &\geq S(Z|E) - S(Z|B) \\ &\geq \left[\log_2 \frac{1}{C} - S(X|B) \right] - S(Z|B). \end{aligned} \quad (3)$$

Both parties involved in the HD-BB84 protocol utilize complete bases elements (Z and X bases) within a d -dimensional Hilbert space. In this context, the lower limit for parameter estimation can be directly achieved from Fano's inequality. It is possible to consider an arbitrary quantum channel with a noise probability denoted as q . Fano's inequality states that $S(Z|B) \leq h(q) + q \log_2(d-1)$. By applying this relation in Eq. (3) and considering the condition that $\log_2 \frac{1}{C}$ cannot exceed $\log_2 d$, we can derive

$$r \geq \log_2 d - 2(h(q) + q \log_2(d-1)). \quad (4)$$

For the binary encoding and decoding scheme the conditional entropy of Alice's measurement outcome given Bob's measurement result is equal to $h(\varepsilon)$, where ε is quantum bit error rate (QBER) [147, 148]. Here, q is the depolarizing channel parameter i.e., the probability that outcome of the Z by Alice and Bob is not equal and h is binary entropy. Through an examination of the aforementioned formulas, we ascertain the lower bound of the key rate for the HD-BB84 protocol. This analysis involves the application of Fano's inequality, which establishes bound on parameter estimation. Additionally, the determination of the QBER is crucial for enhancing negotiation efficiency, thereby playing a pivotal role in augmenting the overall security and correctness of the final key in the HD-BB84 protocol.

Before delving into the formal analysis of the aforementioned formalism, it is crucial to elucidate the relationship among key rate, QBER, noise and negotiation efficiency. The noise introduced in the quantum channel (q), results in QBER (ε) in the raw key sequence after executing the quantum protocol. The conditional entropy of Alice's measurement outcome given Bob's measurement outcome, as well as the conditional von Neumann entropy of Alice's quantum state given Bob's quantum state, can be expressed as functions of ε . Additionally, it is evident that the conditional entropy is directly influenced by the noise in the quantum channel. We may now explicitly analyze the previously mentioned formulae, considering negotiation efficiency and QBER within the key rate equation. First, we need to elaborate on all the elements in Eq. (1). From Appendix A, $S(a|E)$ represents the conditional von Neumann entropy, defined as follows:

$$S(a|E) \geq \sum_{c \neq m, c \neq n} \left(\frac{K_c^0 + K_c^1}{M} \right) S_c + \left(\frac{K_m^0 + K_m^1}{M} \right) S_m + \left(\frac{K_n^0 + K_n^1}{M} \right) S_n,$$

where,

$$\begin{aligned} K_c^0 &:= \langle E_c^m | E_c^m \rangle, & K_c^1 &:= \frac{1}{2} \langle F_c | F_c \rangle, \forall c \neq m, n \\ K_m^0 &:= \frac{1}{4} \langle E_m^m | E_m^m \rangle, & K_m^1 &:= \frac{1}{8} \langle F_m | F_m \rangle, \\ K_n^0 &:= \frac{3}{4} \langle E_n^m | E_n^m \rangle, & K_n^1 &:= \frac{3}{8} \langle F_n | F_n \rangle. \end{aligned}$$

and

$$\begin{aligned} S_c &= h\left(\frac{K_c^0}{K_c^0 + K_c^1}\right) - h\left(\frac{1}{2} + \frac{\sqrt{(K_c^0 - K_c^1)^2 + 4 \operatorname{Re}^2 \langle E_c^m | \frac{1}{\sqrt{2}} F_c \rangle}}{2(K_c^0 + K_c^1)}\right), \\ S_m &= h\left(\frac{K_m^0}{K_m^0 + K_m^1}\right) - h\left(\frac{1}{2} + \frac{\sqrt{(K_m^0 - K_m^1)^2 + 4 \operatorname{Re}^2 \langle \frac{1}{2} E_m^m | \frac{1}{2\sqrt{2}} F_m \rangle}}{2(K_m^0 + K_m^1)}\right), \\ S_n &= h\left(\frac{K_n^0}{K_n^0 + K_n^1}\right) - h\left(\frac{1}{2} + \frac{\sqrt{(K_n^0 - K_n^1)^2 + 4 \operatorname{Re}^2 \langle \frac{3}{4\sqrt{2}} E_n^m | F_n \rangle}}{2(K_n^0 + K_n^1)}\right). \end{aligned}$$

⁶ Eve performs an entanglement operation using her ancillary state E with Alice's state (A) and Bob's quantum memory (B).

Further, $H(a|b)$ represents the conditional entropy of Alice's measurement outcome given Bob's measurement outcome, defined as follows:

$$H(a|b) = H(p_{00}, p_{01}, p_{10}, p_{11}) - h(p_{00} + p_{10}).$$

We have previously defined the values p_{00}, p_{01}, p_{10} and p_{11} (also detailed in Appendix A) through the analysis of parameter estimation for the HD-Ext-B92 protocol. These terms depend on q . Moreover, for binary encoding and decoding, $H(a|b) \equiv h(\varepsilon)$. Therefore, it can be concluded that the conditional entropy and key rate depend on the value of ε and, consequently, on q as ε depends on q . Now, if we incorporate negotiation efficiency⁷ (ξ) into the key rate for the HD-Ext-B92 protocol (as shown in Eq. (1)), the secure key rate equation can be written as,

$$R_\xi \equiv \xi R(a, b, E) = \xi (\inf [S(a|E) - H(a|b)]).$$

Here, $H(a|b)$ depends on noise and the QBER value. To reduce QBER, legitimate users perform error correction and privacy amplification, which increase the mutual information between Alice and Bob. This leads to a decrease in $H(a|b)$ and maximizes the proportion of raw key bits successfully converted into secure key bits. Therefore, analyzing QBER of a quantum protocol enhances the *correctness* and *security* of the raw key and optimizes the conversion of raw key into secure key more efficiently, thereby improving the negotiation efficiency. The QBER analysis during the test rounds is a crucial aspect of quantum communication protocols, as it helps to improve negotiation efficiency. This logic applies similarly to the HD-BB84 protocol. From Eqs. (3) and (4), it is clear that the conditional von Neumann entropy $S(Z|B)$ depends on q (as Fano's inequality states that $S(Z|B) \leq h(q) + q \log_2(d-1)$), which affects the QBER value as well. Considering negotiation efficiency in the key rate for the HD-BB84 protocol (Eq. (4)), the secure key rate equation can be expressed as follows:

$$r_\xi \equiv \xi r \geq \xi (\log_2 d - 2(h(q) + q \log_2(d-1))).$$

Here, the legitimate parties perform parameter estimation and error correction on the raw key sequence, which leads to a reduction in QBER and a decrease in $S(Z|B)$. As a result, the key rate increases. Consequently, this process increases the proportion of raw key bits that are successfully converted into secure key bits. More specifically, analyzing the QBER during the test rounds of a quantum communication protocol improves the correctness and security of the raw key, making the conversion process to secure key more efficient. This optimization of the secure key conversion improves the negotiation efficiency, ξ . From this analysis, we can conclude that QBER analysis is crucial for improving the negotiation efficiency of a quantum protocol.

The preceding discussion, along with an analysis of the formulations, elucidates that Eq. (1), which incorporates Eqs. (18) and (19) from Appendix A, and Eq. (4), representing the key rate formula for HD-Ext-B92 and HD-BB84 protocols, inherently encompasses the essential steps of parameter *negotiation efficiency*. By employing these key rate equations, coupled with the transmittance in satellite-based communication (cf. Eqs. (5) and (8)), we can derive the average key rate for LEO satellite-based quantum communication. The computation of the average key rate using Eq. (9) facilitates the determination of the probability distribution of key rates and the variation of key rates concerning various parameters in satellite quantum communication, as detailed in Section III. Before delving further this section, we conduct an in-depth analysis of these key rate equations for both HD-QKD protocols in the subsequent paragraph. Before proceeding, it is crucial to emphasize the definition of noise tolerance and its relationship with QBER. Noise tolerance in a quantum communication protocol refers to the ability of the protocol to function correctly and securely despite the presence of noise. Specifically, the value of noise tolerance for a protocol is determined by the point at which the secure key rate approaches zero. Noise can originate from various sources, including environmental disturbances, imperfections in quantum devices, and potential eavesdropping activities. Noise tolerance and QBER are interdependent factors in quantum communication protocols. Effective noise management ensures that QBER remains below the critical threshold, thereby enabling secure and efficient quantum communication. Error correction techniques are employed to correct errors in the raw key, and their efficiency depends on the QBER. Higher QBER necessitates more robust error correction, which can diminish the efficiency of the key generation process. Privacy amplification is used to reduce the information an eavesdropper (Eve) might have obtained; the amount of privacy amplification required increases with higher QBER⁸, further reducing the final key length. Maintaining noise within

⁷ Negotiation efficiency is defined as the effectiveness with which the steps involved in establishing a secure key are executed. These steps generally encompass sifting, error correction and privacy amplification. High negotiation efficiency indicates that these processes are conducted in a way that optimizes the conversion of raw key bits into secure key bits [134, 135, 138].

⁸ A detailed analysis of privacy amplification and error correction is beyond the scope of the current work.

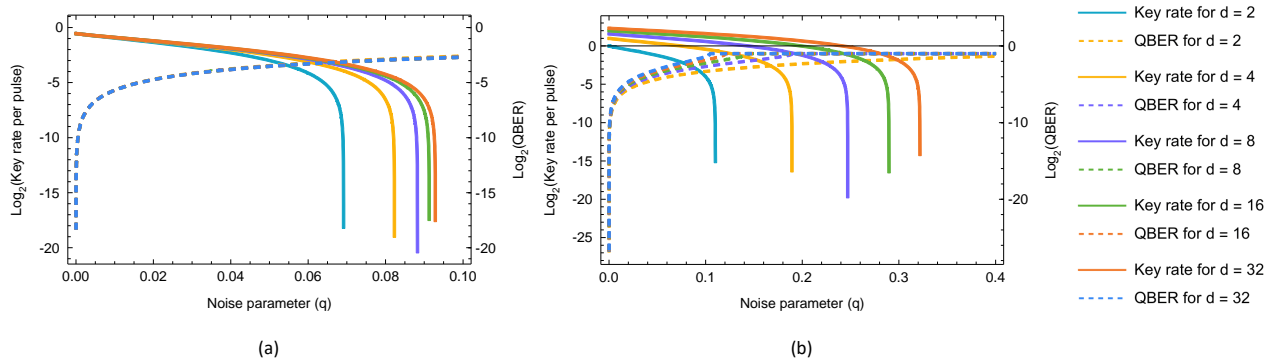


Figure 1. (Color online) Plot of variation of key-rate and QBER with channel noise parameter (both plots share a common legend): (a) key-rate and QBER analysis of HD-Ext-B92 protocol with noise parameter (q) for different dimensions in Hilbert space (the plot lines representing QBER for all dimensions are superimposed), (b) key-rate and QBER analysis of HD-BB84 protocol with noise parameter (q) for different dimensions in Hilbert space.

the noise tolerance limit helps to keep QBER below a secure threshold value, which is specific to the protocol. In such cases, extensive privacy amplification and error correction may not be strictly necessary.

To analyze the behavior of the key rate per pulse and the QBER concerning the noise parameter in both the above-discussed HD protocols, we utilize the key rate equations (refer to Eqs. (1), (4), and Appendix A) and the binary QBER function ($h(\epsilon)$). Now, we analyze the result illustrated in Figure 1 for HD-Ext-B92 and HD-BB84 schemes. We can observe in the HD-Ext-B92 protocol that events with mismatched bases are not disregarded, which occurs when Alice and Bob employ different measurement bases. These events can significantly enhance key generation rates [110, 149–152], and therefore noise tolerance is also increased for this scheme which is evident from the graph. We plot the variation of the key rate of HD-Ext-B92 protocol with noise parameter (q) in a depolarizing channel in the d -dimensional Hilbert space; we also depict the variation of QBER with the same noise parameter (q). It may be observed that as the value of d increases, the tolerance for noise also increases, showing a rise from 7% to 10%. It is apt to note that, the maximum tolerable noise is dependent on the choice of both the depolarizing channel and of Eve's ancilla state, since, these two factors significantly impact parameter estimation and consequently affect the key rate. Nevertheless, our analysis is confined to a specific choice of these two factors, which have been outlined in Appendix A. In Figure 1 (a), it becomes evident that the QBER remains constant across different d values. The plots representing the distinct d values (i.e., $d = 2, 4, 8, 16, 32$) overlap in QBER analysis, indicating consistent outcomes for higher-dimensional cases of the HD-Ext-B92 protocol. Additionally, the graph (represented by a dotted line) demonstrates that the QBER reaches a saturation point for a particular q value (for HD-Ext-B92). We have computed the initial point where the QBER begins to rise for various q values and observed a physically reasonable variation. For instance, when q is ~ 0.005 , the QBER is approximately 0.015. As the q value increases to ~ 0.1 , the QBER saturates at approximately 0.088. Now, we analyze the plots for HD-BB84 in Figure 1 (b) and undertake a comprehensive comparison with HD-Ext-B92. A numerical assessment reveals that the key rate increases as the value of d rises for HD-BB84. Conversely, in HD-Ext-B92, the minimum key rate remains fairly consistent for all d values which is around 0.7. Further, the noise tolerance is increased significantly with a greater value of d in HD-BB84. For instance, the tolerable noise is $\sim 11\%$ for $d = 2$ (for qubit) and with the increased value of $d = 32$, this limit increases to $\sim 32\%$. More simply, the HD-Ext-B92 protocol operates securely and correctly with a maximum noise tolerance ranging from 7% to 10%, whereas the HD-BB84 protocol can tolerate up to 11% noise for $d = 2$ and up to 32% noise for $d = 32$, as can be inferred from Eq. (4). This outcome demonstrates the advantage of opting for the HD-BB84 protocol over HD-Ext-B92 when considering aspects like key rate and noise tolerance. HD-BB84 surpasses the HD-Ext-B92 protocol. It is worth mentioning that in the original scheme of HD-Ext-B92 [110], authors do not employ two complete bases as HD-BB84 does. In their approach, they utilize a simplified version in which Alice's requirement is reduced to transmitting just three states, and Bob only needs to carry out partial measurements within the second basis [110]. Additionally, it is important to highlight that they did not select an optimal basis configuration. Alternate choices for the encoding state might yield greater key rates for the HD-Ext-B92 protocol, as shown in cases involving qubits [101, 142]. If we examine the QBER aspect within the context of HD-BB84, it becomes apparent that the variation of QBER with the noise parameter (q) rapidly converges to a saturation value (~ 0.25) as the dimension of qudit increases. In contrast to the HD-Ext-B92 protocol, the susceptibility of QBER to noise is notably more vulnerable in the HD-BB84 protocol. Moreover, as depicted in Figure 1, when considering $d = 32$, the saturation point of noise tolerance is attained in the HD-Ext-B92 protocol. In contrast, in the HD-BB84 protocol, the rate at which noise

tolerance increases becomes progressively lower as d increases. It is noteworthy that at $d = 32$, the QBER has not yet reached its saturation point (for HD-BB84); this point will be reached at higher values of d . From Figure 1 (b), we observe that when the key rate reaches zero, it indicates the noise tolerance values, q , with QBER lines reaching their maximum value for the respective dimensions. The conditional entropy of Alice's measurement outcome given Bob's measurement outcome (and the conditional von Neumann entropy of Alice's quantum state given Bob's quantum state) is directly influenced by the noise in the quantum channel. These conditional entropies can be expressed as function of QBER. Mathematically, the relationship between noise tolerance and QBER in a quantum communication protocol is illustrated by the effect of QBER on the secure key rate. A protocol has a capability to handle noise up to a specific QBER threshold, allowing error correction and privacy amplification to still generate a secure key. The binary entropy function $h(\text{QBER})$ and the specific security function $f(\text{QBER})$ measure the information loss due to errors and potential eavesdropping, respectively.

B. Satellite-based optical links: model used for the elliptic beam approximation

In this article, we aim to analyze the performance of key rates in various situations of HD-Ext-B92 and HD-BB84 protocols. The channel transmission η for the light propagation through atmospheric links using elliptic-beam approximation as introduced by Vasylyev et al. [111, 112] will be employed to perform the analysis. Further, in what follows, we impose the generalized approach⁹ and different weather conditions as introduced in [113]. This method yields an impact on the value of transmittance as the transmittance is determined by beam parameters along with the diameter of the receiving aperture. To provide readers with a clearer understanding of both the elliptic beam approximation and its modified version in a more comprehensive manner, in this section, we offer a succinct explanation of the underlying theory.

Temporal and spatial fluctuations in temperature and pressure within turbulent atmospheric flows result in random variations of the air's refractive index. Consequently, the atmosphere introduces losses to transmitted photons, which are detected at the receiver through a detection module featuring a limited aperture. The transmitted signal undergoes degradation due to phenomena like beam wandering, broadening, deformation, and similar effects. We can examine this scenario by focusing on a Gaussian beam propagating along the z axis, reaching the aperture plane positioned at a distance $z = L$. In this analysis, we observe that assuming perfect Gaussian beams emitted by the transmitter is not entirely realistic. Standard telescopes typically produce beams with intensity distributions that closely resemble a circular Gaussian profile with some deviations, often caused by truncation effects at the edges of optical elements. One notable consequence of these imperfections is the inherent broadening of the beam due to diffraction. In our model, we can address this phenomenon by adjusting the parameter representing the initial beam width (\mathcal{W}_0), thereby accounting for the increased divergence in the far-field resulting from the imperfect quasi-Gaussian beam. To capture this effect, we incorporate the transmission of the elliptical beam through a circular aperture and consider the statistical characteristics of the elliptical beam as it propagates through turbulence using a Gaussian approximation. However, it's important to mention certain restriction for simplifications in our approach, particularly the assumption of isotropic atmospheric turbulence. For a more detailed formulation, readers are referred to the Supplemental Material of Ref. [111]. That quasi-Gaussian beam is directed through a link that spans both the atmosphere and vacuum, originating from either a transmitter situated in orbit or a ground station. The link is characterized by non-uniform conditions. Generally, the varying intensity transmittance of such a signal (received beam) via a circular aperture of radius r of the receiving telescope is expressed as follows [111, 153]:

$$\eta = \int_{|\rho|^2=r^2} d^2\rho |u(\rho, L)|^2, \quad (5)$$

where $u(\rho, L)$ represents the beam envelope at the receiver plane, located at a distance L from the transmitter, and $|u(\rho, L)|^2$ is the normalized intensity with respect to full ρ plane, where ρ denotes the position vector within the transverse plane. The vector parameter \mathbf{v} fully characterizes the state of the beam at the receiver plane (see Figure 2),

$$\mathbf{v} = (x_0, y_0, \mathcal{W}_1, \mathcal{W}_2, \varphi), \quad (6)$$

$x_0, y_0, \mathcal{W}_{1/2}$, and φ imply the beam centroid coordinates, the principal semi-axes of the elliptic beam profile, and the orientation angle of the elliptic beam, respectively. The transmittance is determined by these beam parameters along with the radius of the receiving aperture (r).

⁹ Using non-uniform link between a satellite and the ground station, referred to in Eq. (7).

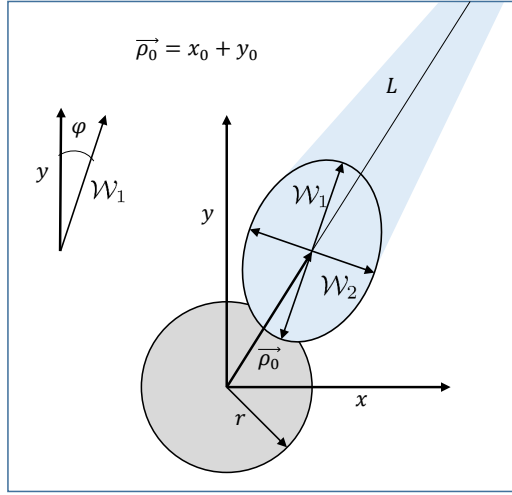


Figure 2. (Color online) Diagram illustrating the received beam and the receiving aperture. L is the total link-length in the propagation direction, r represents the radius of the receiving aperture, $\rho_0 = (x_0, y_0)$ signifies the position of the beam centroid, W_1 and W_2 are the principal semi axes of elliptic beam profile, and φ is the orientation angle of the elliptic beam.

In general, the atmosphere can be categorized into distinct layers, each characterized by various physical parameters such as air density, pressure, temperature, the presence of ionized particles, and more. The arrangement of these layers varies according to location, particularly concerning the extent of each layer's thickness. Without loss of generality, we adopt a simplified model of a satellite-based optical link [113]. This model entails a uniform atmosphere up to a specific altitude denoted as \bar{h} , beyond which a vacuum extends all the way to the satellite situated at an altitude marked as \bar{L} , as illustrated in Figure 3. Rather than dealing with a continuous range of values characterizing physical quantities as a function of altitude, this approach involves just two key parameters. These parameters encompass the value of the physical quantity within the uniform atmosphere and the effective altitude range, \bar{h} . This simplification is likely to be quite accurate because atmospheric influences are predominantly significant only within the initial 10 to 20 kilometers above the Earth's surface. This is particularly relevant considering that the standard orbital height for LEO satellites is above 400 kilometers. In our analysis, we set the value of \bar{L} to 500 km, and assume that the zenith angle falls within the range of $[0^\circ, 80^\circ]$. Under these conditions, the range of the satellite's orbit suitable for key distribution is approximately $L \in [500, 2000]$ km¹⁰. The given context mandates that the effective atmospheric thickness \bar{h} remains constant at 20 km, by the aforementioned factors. We extend the discussion by maintaining the premise that the parameters quantifying the influence of atmospheric effects remain constant (with values greater than 0) within the atmosphere and are set to 0 outside it. In this context, we can make use of the assumption that,

$$\begin{aligned} \text{Down-link} & \begin{cases} C_n^2(z) &= C_n^2 \Omega(z - (L - h)), \\ n_0(z) &= n_0 \Omega(z - (L - h)), \end{cases} \\ \text{Up-link} & \begin{cases} C_n^2(z) &= C_n^2 \Omega(h - z), \\ n_0(z) &= n_0 \Omega(h - z). \end{cases} \end{aligned} \quad (7)$$

Here, C_n^2 represents the refractive index structure constant¹¹, and n_0 denotes the density of scattering particles [158, 159]. The function $\Omega(z)$ corresponds to the Heaviside step-function¹². As stated above, the parameter z signifies the longitudinal coordinate, while L stands for the overall length of the link. Additionally, h represents the distance covered within the atmosphere, as illustrated in the accompanying Figure 3.

Now, let's consider the transmittance, as defined in Eq. (5), for an elliptic beam that strikes a circular aperture with a radius of r . This transmittance can be expressed as follows [111]:

¹⁰ The correlation between total link length and zenith angle is, $L = \bar{L} \sec \phi$.

¹¹ Several altitude-dependent models describing the refractive index structure constant C_n^2 have been documented [154–157]. Among these, the parametric fit proposed by Hufnagel and Valley is widely adopted and faithfully captures the characteristics of C_n^2 in climates characteristic of mid-latitudes [154, 155].

¹² The value of this function is zero for negative arguments and one for positive arguments. This function falls within the broader category of step functions.

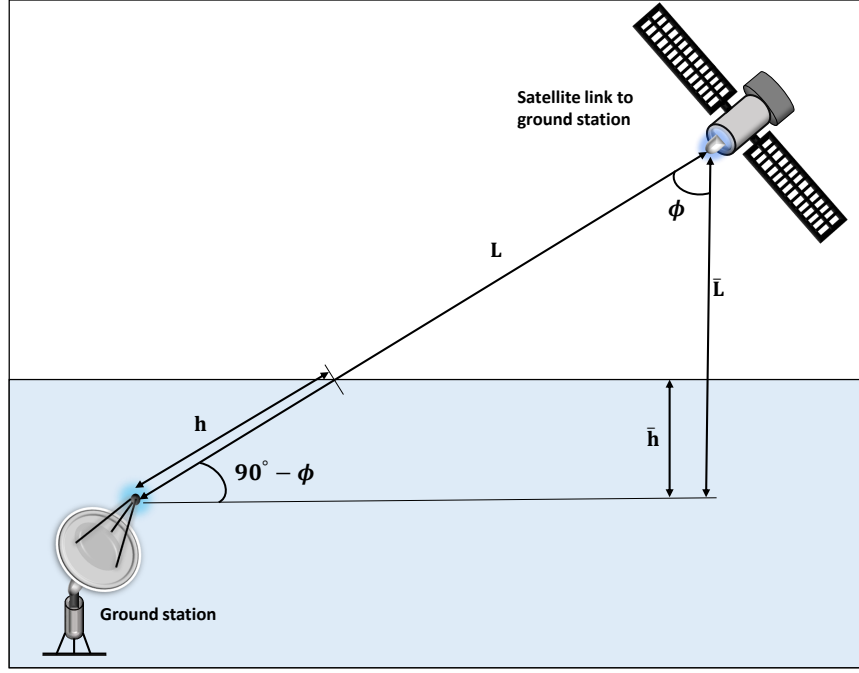


Figure 3. (Color online) This figure depicted that the non-uniform free-space link between the satellite and the ground station. The diagram highlights key parameters, \bar{h} is the thickness of the atmosphere, \bar{L} is the altitude of the satellite, h represents length of the propagation of light inside atmosphere, L is the link length between satellite and ground station, ϕ denotes the zenith angle. Up-link (down-link) configuration represents the transmission of light from ground station to satellite (satellite to ground station).

$$\eta(x_0, y_0, \mathcal{W}_1, \mathcal{W}_2, \varphi) = \frac{2\chi_{\text{ext}}}{\pi\mathcal{W}_1\mathcal{W}_2} \int_0^r \rho d\rho \int_0^{2\pi} d\theta e^{-2A_1(\rho\cos\theta - \rho_0)^2} e^{-2A_2\rho^2\sin^2\theta} e^{-2A_3(\rho\cos\theta - \rho_0)\rho\sin\theta}. \quad (8)$$

In this context, r represents the radius of the aperture, while ρ and θ denote the polar coordinates of the vector $\boldsymbol{\rho}$,

$$\begin{aligned} x &= \rho \cos\theta, \\ y &= \rho \sin\theta, \end{aligned}$$

here, ρ_0 and θ_0 represent polar coordinates corresponding to the vector $\boldsymbol{\rho}_0$,

$$\begin{aligned} x_0 &= \rho_0 \cos\theta_0, \\ y_0 &= \rho_0 \sin\theta_0, \end{aligned}$$

and

$$\begin{aligned} A_1 &= \left(\frac{\cos^2(\varphi - \theta_0)}{\mathcal{W}_1^2} + \frac{\sin^2(\varphi - \theta_0)}{\mathcal{W}_2^2} \right), \\ A_2 &= \left(\frac{\sin^2(\varphi - \theta_0)}{\mathcal{W}_1^2} + \frac{\cos^2(\varphi - \theta_0)}{\mathcal{W}_2^2} \right), \\ A_3 &= \left(\frac{1}{\mathcal{W}_1^2} - \frac{1}{\mathcal{W}_2^2} \right) \sin 2(\varphi - \theta_0). \end{aligned}$$

These expressions can be employed for numerical integration, as described in Eq. (8), through the Monte Carlo method or another effective technique for the same purpose. To simplify the process of integration using the Monte Carlo method, it requires the generation of N sets of values for the vector \boldsymbol{v} (see Eq. (6)). It is assumed that the angle $(\varphi - \theta_0)$ follows a uniform distribution over the interval $[0, \frac{\pi}{2}]$ and other parameters¹³ $(x_0, y_0, \Theta_1, \Theta_2)$ follow

¹³ To compute transmittance, first one has to evaluate \mathcal{W}_i from Θ_i using relation $\Theta_i = \ln\left(\frac{\mathcal{W}_i^2}{\mathcal{W}_0^2}\right)$, $i = 1, 2$. Here, \mathcal{W}_0 is the beam spot radius at the transmitter.

the normal distribution [160]. Substitution of the simulated values of \mathbf{v} into Eq. (8) makes it feasible to perform the numerical integration. The outcome of this process also involves the *extinction factor*¹⁴, χ_{ext} , thereby producing N atmospheric transmittance values, denoted as $\eta(\mathbf{v}_i)$, where i ranges from 1 to N . The necessary parameters for simulation are described in Appendix B which are calculated according to our model. These expressions are different for up-link and down-link configuration as different expressions mentioned in Eq. (7) are used for up-link and down-link configuration.

In the next section, we will evaluate the effectiveness of the HD protocols selected by us in the satellite-based links. To conduct this assessment, we need average key rates over the probability distribution of the transmittance (PDT)¹⁵ computed for different link lengths and configurations. The same can be expressed as [113],

$$\bar{R} = \int_0^1 R(\eta) P(\eta) d\eta = \sum_{i=1}^{N_{bins}} R(\eta_i) P(\eta_i), \quad (9)$$

where, \bar{R} represents the average key rate, while $R(\eta)$ signifies the key rate corresponding to a specific transmittance value. The PDT is denoted as $P(\eta)$. To compute the integral average, the interval $[0, 1]$ is divided into N_{bins} bins, each centered at η_i for i ranging from 1 to N_{bins} , and is evaluated by combining the weighted sum of the rates. The estimation of $P(\eta_i)$ relies on random sampling, as explained in the earlier paragraph. The formulations for the distinct implementations key rates $R(\eta)$ can be found in Section II A.

III. PERFORMANCE ANALYSIS OF PROTOCOLS AFTER SIMULATION

In this section, we elaborately analyze the impact of PDT¹⁶ on key rate after the weighted sum, as well as the probability distribution of key rate (PDR) concerning the HD-Ext-B92 and HD-BB84 protocols. The minimum separation between Alice and Bob (i.e., altitude of the satellite) remains constant at a distance of $L = 500$ km, as the primary focus is on scenarios involving LEO satellites like the Chinese satellite Micius [78, 79, 83, 84]. We present outcomes of numerical simulation for satellite-based HD-Ext-B92 and HD-BB84 schemes under asymptotic conditions. The simulation incorporates the experimental parameters outlined in Table I [113, 162, 163]. The parameters C_n^2 , n_0 , and h are typically determined by fitting experimental data. However, for the sake of establishing a predictive model, we parameterize these values in a rational manner. We conduct simulations under varying atmospheric conditions, encompassing clear, slightly foggy, and moderately foggy nights, as well as non-windy, moderately windy, and windy days [113]. A particularly noteworthy aspect is the comparison between nighttime and daytime operations. In daytime conditions, elevated temperatures result in stronger winds and heightened mixing across atmospheric layers, leading to more pronounced turbulence effects and consequently higher values of C_n^2 compared to nighttime conditions. Nevertheless, on average, during clear days, the lower atmosphere exhibits reduced moisture content compared to nighttime, resulting in diminished beam spreading due to scattering particles. Conversely, nighttime conditions, characterized by lower temperatures, yield a less turbulent atmosphere. Additionally, the formation of haze and mist contributes to higher values of n_0 compared to daytime conditions. In such scenarios, the impact of scattering over particulate matter can surpass the effects induced by turbulence. The crucial factors in this scenario include not only those associated with atmospheric influences but also the radii of the transmitting and receiving telescopes, along with the wavelength of the signal. For the satellite in orbit, we opted for a radius of $r_{\text{sat}} = 15$ cm (\mathcal{W}_0), while the ground station telescope has a radius of $r_{\text{grnd}} = 0.5$ m, and the signal wavelength is $\lambda = 785$ nm. Based on Eq. (7), it is evident that a down-link pertains to satellite-to-ground communication, where atmospheric effects become significant only in the latter part of the propagation process, i.e., when z exceeds $(L - h)$. On the other hand, for up-links, these effects are relevant only when z is below h .

From Appendix B, it becomes evident, as expected that the impact of atmospheric effects is considerably more pronounced in the case of up-links compared to down-links. The underlying phenomena at play here, namely beam deflection and broadening, encompass angular effects. These effects play a role in determining the ultimate size of the beam, thus influencing the channel losses. Their magnitude is directly proportional to the distance covered after the initiation of the effect known as *kick in effect*. For up-links, these effects manifest near the transmitter, resulting in beam broadening spanning hundreds of kilometers before detection at the satellite. Conversely, in the down-link scenario, the majority of the beam's trajectory occurs within a vacuum, with atmospheric effects coming into play

¹⁴ The parameter $\chi_{\text{ext}}(\phi)$ denotes the extinction losses caused by atmospheric back-scattering and absorption. It varies depending on the elevation angle ($90^\circ - \phi$) or zenith angle (ϕ) [114, 161].

¹⁵ Some authors followed the relation $\eta_\delta = 10^{-\frac{\delta}{10}}$ with $\delta = \alpha_1 L$ [dB] to represent the channel transmittance with the form of attenuation, here, L total link length and α_1 is loss in the channel transmission dB/km.

¹⁶ See PDT in Figures 3 and 4 in Ref. [113] after random sampling of beam parameters \mathbf{v} for a down-link and an up-link, respectively.

Parameter	Value	Short description
\mathcal{W}_0	15 cm, 50 cm	Down-link, up-link
r	50 cm, 15 cm	Down-link, up-link
λ	785 nm	Wavelength of the signal light
β	0.7	Parameter in $\chi_{\text{ext}}(\phi)$
α	2×10^{-6} rad	Pointing error
\bar{h}	20 km	Atmosphere thickness
\bar{L}	500 km	Minimum altitude (at zenith)
n_0	0.61 m^{-3}	Night-time condition 1
n_0	0.01 m^{-3}	Day-time condition 1
n_0	3.00 m^{-3}	Night-time condition 2
n_0	0.05 m^{-3}	Day-time condition 2
n_0	6.10 m^{-3}	Night-time condition 3
n_0	0.10 m^{-3}	Day-time condition 3
C_n^2	$1.12 \times 10^{-16} \text{ m}^{-\frac{2}{3}}$	Night-time condition 1
C_n^2	$1.64 \times 10^{-16} \text{ m}^{-\frac{2}{3}}$	Day-time condition 1
C_n^2	$5.50 \times 10^{-16} \text{ m}^{-\frac{2}{3}}$	Night-time condition 2
C_n^2	$8.00 \times 10^{-16} \text{ m}^{-\frac{2}{3}}$	Day-time condition 2
C_n^2	$1.10 \times 10^{-15} \text{ m}^{-\frac{2}{3}}$	Night-time condition 3
C_n^2	$1.60 \times 10^{-15} \text{ m}^{-\frac{2}{3}}$	Day-time condition 3

Table I. Parameters associated with the optical and technical characteristics of the link and different atmospheric weather conditions.

only during the final fifteen to twenty kilometers before reaching the receiver. A secondary distinction lies in the origin of fluctuations in the position of the beam centroid, denoted as (x_0, y_0) . In up-links, the atmosphere-induced deflections tend to be significantly more influential than pointing errors (φ), which is disregarded. On the other hand, in down-links, the beam dimensions are already substantially larger than any turbulent irregularities at the top of the atmosphere. As a consequence, the resulting beam wandering due to atmospheric effects can be neglected, rendering pointing errors the dominant contributing factor.

Utilizing Equation (1), which integrates Equations (18) and (19) from Appendix A, and Eq. (4), which represent as the key rate formula for HD-Ext-B92 and HD-BB84 protocols, along with PDT in satellite-based communication (refer to Eqs. (5) and (8)), enables the computation of the average key rate for LEO satellite quantum communication. Employing Eq. (9) in this calculation facilitates the determination of the probability distribution of key rates and the assessment of key rate variations with respect to different parameters in the context of satellite quantum communication. Now, we aim to investigate the average key rate as a function of zenith angle, considering minimal noise. Figures 4 illustrate the average key rate using the PDT concerning the angle relative to the zenith. This analysis is carried out for both up-links and down-links across various weather conditions for dimension¹⁷, $d = 32$ (see Table I). Each data point on the graph is derived from 10,000 parameter samples in Eq. (6) and computed using Eq. (8). In Figures 4 (a) and 4 (b), the graphs reveal that during daytime condition 1, the highest average key rate is yielded in the zenith position (~ 0.0012 and ~ 0.008) for HD-Ext-B92 and HD-BB84 protocols, respectively, in the up-link configuration. Notably, the key rate¹⁸ is slightly greater for HD-BB84 which corresponds to the expected result. For the same configuration, the key rate sharply diminishes under other conditions (Day 2 and Night 1-2). Comparatively, for HD-Ext-B92, the maximum value of the key rate (~ 0.0002) is nearly ten times lower than that of the HD-BB84 protocol (~ 0.002) corresponding to the day condition 2. A similar comparison holds for night 1/2 conditions. For these conditions, the key rate becomes approximately zero at zenith angle 50° . It may be noted that in night-time condition 1, the key rate is lower than in day-time condition 2 for both schemes within the same configuration. Based on these observations, we can infer that daytime transmission in the up-link configuration performs more favorably than nighttime transmission. Due to the very low key rate during night-time condition 2, we have chosen to negate condition 3, both in night-time and day-time, from the graphical representation. Additionally, in the up-link configuration, the simulation results reveal a tenfold disparity in key rates between HD-Ext-B92 and HD-BB84 during day-time condition 2. In contrast, during day-time condition 1, the difference is less pronounced, approximately five fold. This discrepancy is attributed to the non-windy nature of day-time condition 1, while day-time condition 2 experiences moderate wind, resulting in a lower value of C_n^2 for the former condition compared to

¹⁷ The weather data information is used from Ref. [113]. We also mention the required information in Table I.

¹⁸ For ease of reference, we will refer to the average key rate as the "key rate".

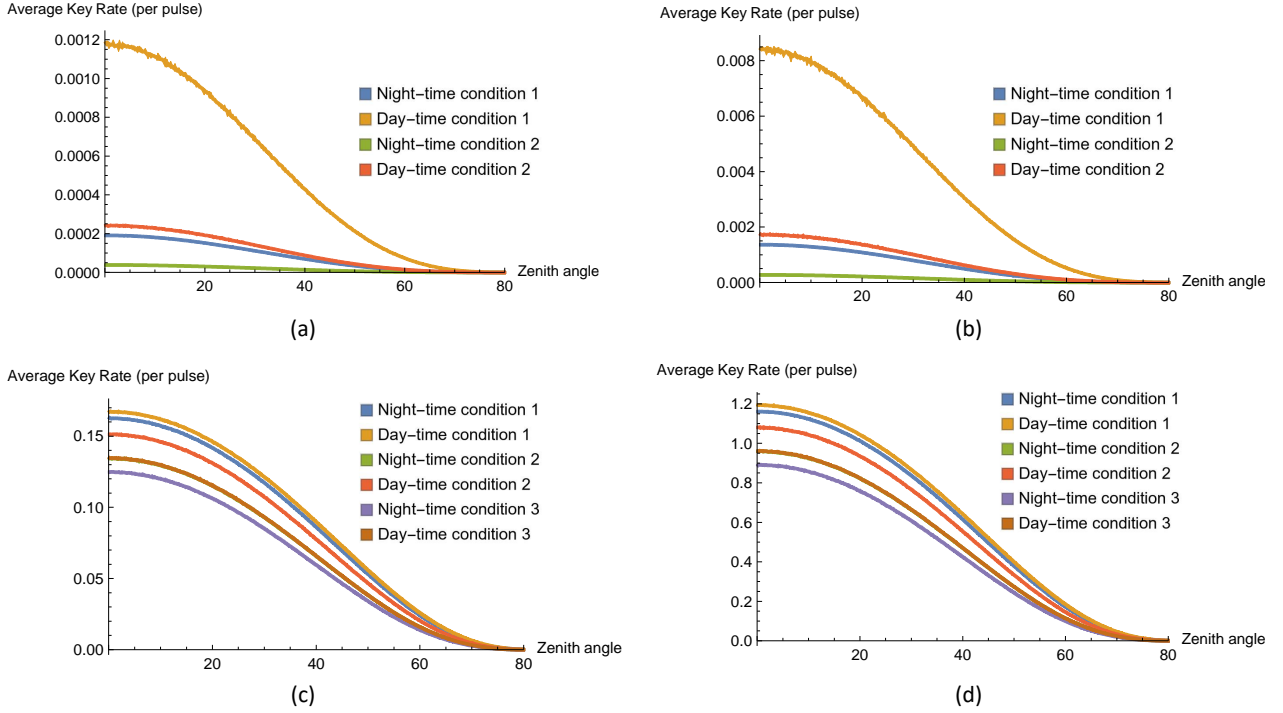


Figure 4. (Color online) Plot of variation of average key rate (per pulse) with zenith angle in different weather conditions considering minimal noise ($d = 32$), i.e., day-time conditions 1, 2 and 3 correspond to not windy, moderate windy and windy, respectively (described as Day-time condition 1/2/3) and night-time conditions 1, 2, 3 correspond to clear, slightly foggy and moderate foggy, respectively (described as Night-time condition 1/2/3). The upper row corresponds to the up-link scenario and the lower row corresponds to the down-link scenario: (a) Average key rate generated by HD-Ext-B92 protocol as a function of zenith angle for up-link configuration under four different weather conditions (Day 1-2 and Night 1-2), (b) Average key rate generated by HD-BB84 protocol as a function of zenith angle for up-link configuration under four different weather condition (Day 1-2 and Night 1-2), (c) Average key rate generated by HD-Ext-B92 protocol as a function of zenith angle for down-link configuration under six different weather condition (Day 1-2-3 and Night 1-2-3), (d) Average key rate generated by HD-BB84 protocol as a function of zenith angle for down-link configuration under six different weather condition (Day 1-2-3 and Night 1-2-3).

the latter. Moreover, the absence of windy conditions indicates a lower moisture content in the lower atmosphere. Consequently, the scattering particle density, denoted as n_0 , is lower in day-time condition 1 compared to day-time condition 2 (see Table I). The down-link configuration is depicted in Figures 4 (c) and 4 (d). As previously discussed, the influence of atmospheric effects is comparatively reduced in the down-link configuration compared to the up-link configuration. Consequently, the performance of the link transmittance is superior for down-link as compared to up-link. This is supported by Figures 4 (c) and 4 (d), which further highlight the enhanced key rate. From these two figures, the overall plot patterns can be seen to be (sequential arrangement of plots representing different weather conditions) consistent for both protocols. The sequence of different weather conditions that yield higher key rate values follows this order: day-time condition 1, night-time condition 1, day-time condition 2, day-time condition 3, night-time condition 2, and night-time condition 3. Additionally, it can be seen that similar to the up-link scenario, the daytime conditions favor channel transmission over the nighttime conditions. This pattern remains consistent across both scenarios. Of particular interest is the comparison between operations during night-time and day-time. During daylight hours, higher temperatures facilitate stronger winds and heightened mixing across distinct atmospheric layers. This generates more prominent turbulence effects. However, on average, clear days witness a reduced moisture content in the lower atmosphere compared to night-time conditions. Consequently, the scattering of particles causes less pronounced beam spreading. Conversely, during night-time, the cooler temperatures result in an atmosphere with lower turbulence levels, coupled with the formation of mist and haze. In such circumstances, scattering tends to have a more substantial impact at night-time than the effects induced by turbulence at day-time. In the down-link scenario, during day-time condition 1, the highest achievable key rates are 0.165 and 1.2 for HD-Ext-B92 and HD-BB84 protocols, respectively. Conversely, in night-time condition 3, the highest attainable key rates are 0.125 and 0.9. The key rate ratio, in the down-link scenario, between the HD-BB84 and HD-Ext-B92 protocols is 7.27 for

the maximum scenario and 7.2 for the minimum scenario. This observation substantiates the anticipated outcome that HD-BB84 consistently outperforms HD-Ext-B92. Furthermore, the key rate decreases significantly within the zenith angle range of 70° to 80° for the down-link scenario, whereas for the up-link scenario, this reduction begins at a zenith angle of 50° . Intuitively, down-link transmission exhibits a higher tolerance for larger zenith angles compared to up-link transmission.

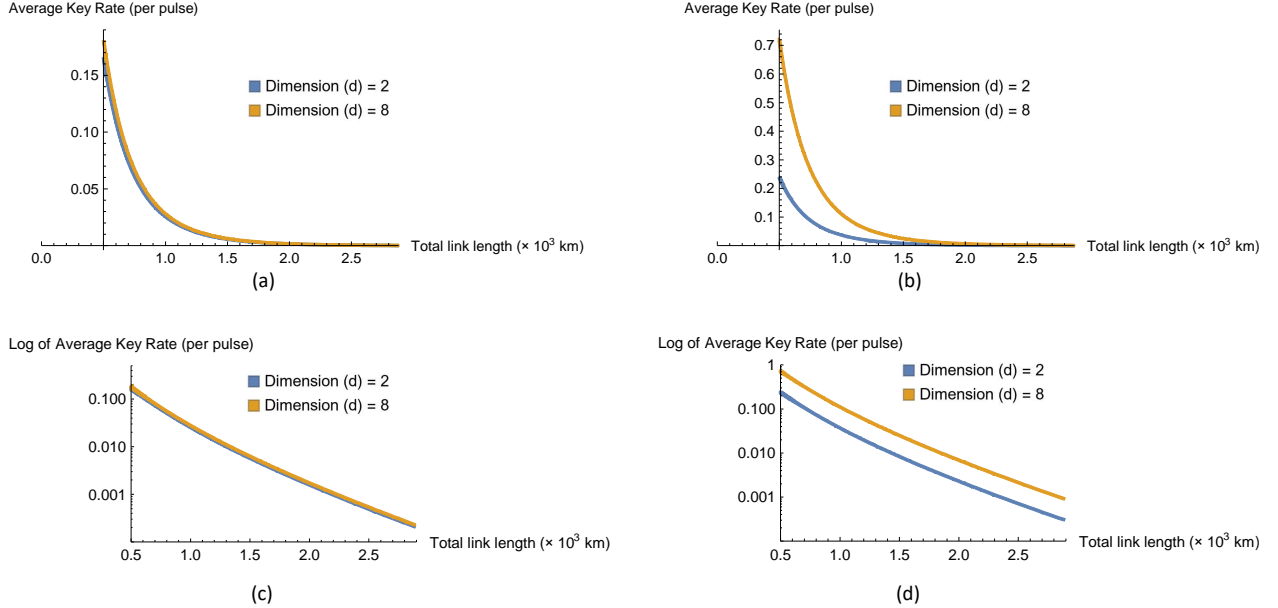


Figure 5. (Color online) Plot of variation of average key rate (per pulse) with total link length under condition Day-1 utilizing different dimensions of qudit ($d = 2$ and $d = 8$): (a) Average key rate generated by HD-Ext-B92 protocol as a function of total link length (L) for down-link configuration, (b) Average key rate generated by HD-BB84 protocol as a function of total link length (L) for down-link configuration, (c) and (d) illustrate the same results as depicted in (a) and (b), respectively, but for a better visualization of the impact of link length on the average key rate, here a logarithmic scale is used along the y -axis.

To obtain the best possible results, hereafter we focus on the down-link configuration under optimal weather conditions where the average key rate is highest (cf. Figure 4). Specifically, we analyze and illustrate the variation of key rate with total link length (L) in day-time condition 1 within down-link configuration, assuming an extremely low noise. In this scenario, the HD-Ext-B92 protocol yields maximum key rates of 0.17 and 0.155 for qudit dimensions 8 and 2, respectively, as illustrated in Figure 5 (a). Notably, the key rate of the HD-BB84 protocol exhibits notable fluctuations across different dimensions. As can be seen from Figure 5 (b), for qudit dimensions 8 and 2, the maximum key rates are 0.7 and 0.24, respectively. Furthermore, the key rate decreases almost linearly for both the HD-QKD protocols and across both dimensions when plotted on a logarithmic scale. Consequently, it can be inferred that the decrease in key rate follows an exponential pattern. Specifically, at a higher zenith angle of 80° , with a total link distance of 2900 km, the key rate of the HD-Ext-B92 protocol is approximately 10^{-4} for both dimensions. In contrast, at the same link distance, the key rates for HD-BB84 are 10^{-3} and 10^{-4} for dimensions 8 and 2, respectively. The HD-BB84 protocol outperforms at higher dimensions, consistent with the findings depicted in the accompanying figure 4.

In Figure 6, we present the PDR with different values of noise parameter (q) at the zenith position ($\phi = 0^\circ$) under down-link configuration. In this context, we employ the optimal performance scenario during day-time condition 1 utilizing qudit dimension of 32. We have used a data set of 10^6 beam parameters to simulate the values of the average key rate and approximate the results to six (five) decimal places¹⁹ to get PDR plots for HD-Ext-B92 (HD-BB84). Within the HD-Ext-B92 protocol, comparing the cases of $q = 0.02$ and $q = 0.06$ (in Figure 6 (a)), we observe a higher key rate for $q = 0.02$, while the maximum value of probability of key rate is greater for $q = 0.06$. The maximum values of probability are consistently greater with greater values of noise parameter. Notably, a higher key rate corresponds to a lower value of probability of occurrence. A specific shape of PDT (as is the case here) implies that the shape of the PDR would remain the same with different noise parameters and different zenith angles (or equivalently with

¹⁹ This is a good choice of approximation to represent, well-suited for PDR representation.

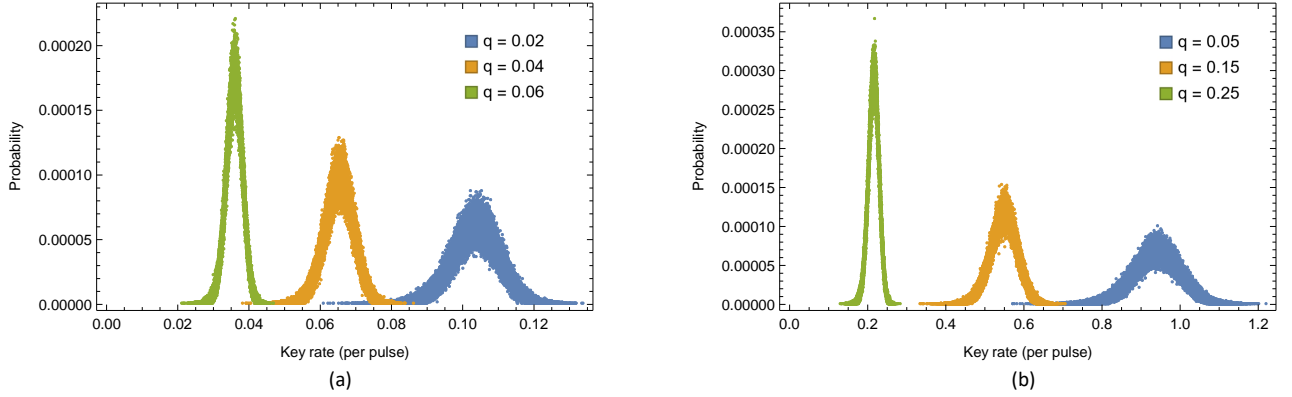


Figure 6. (Color online) Plot of the distribution of key-rate variation for different channel noise parameters (q) at the zenith position under condition Day-1 utilizing qudit of dimension 32: (a) Probability distribution of key-rate for HD-Ext-B92 protocol, (b) Probability distribution of key-rate for HD-BB84 protocol under down-link configuration.

different distances). For example, see that the shape of the PDR remains same for HD-Ext-B92 protocol and HD-BB84 protocol, although the density of data points are more in the case of HD-BB84 (see Figure 6 (a) and (b)). However, this protocol (HD-BB84) exhibits significantly elevated key rate values as well as higher probabilities compared to HD-Ext-B92. Subsequently, we also plot the PDR with different zenith angles in Figure 7, considering extremely low noise characterized by the parameter $q \ll 1$ at the zenith position under condition Day-1 with the same configuration (down-link). Notably, the shapes of the PDR curves remain consistent across both the protocols; however, the data points on the plot appear more densely concentrated in the HD-BB84 protocol. In this case, we have utilized a dataset of 10^6 beam parameters to simulate the values of the average key rate and approximate the results to six (five) decimal places to get PDR plots for HD-Ext-B92 (HD-BB84). The peak values of the probability of key rates in the PDR graph for distinct zenith angles are different for both the protocols. Moreover, for different zenith angles, the peak values of probability in the PDRs are consistently greater in HD-BB84 compared to HD-Ext-B92. In conclusion, we deduce that the PDR curves maintain a uniform shape across varying zenith angles as PDT considered here has a fixed shape.

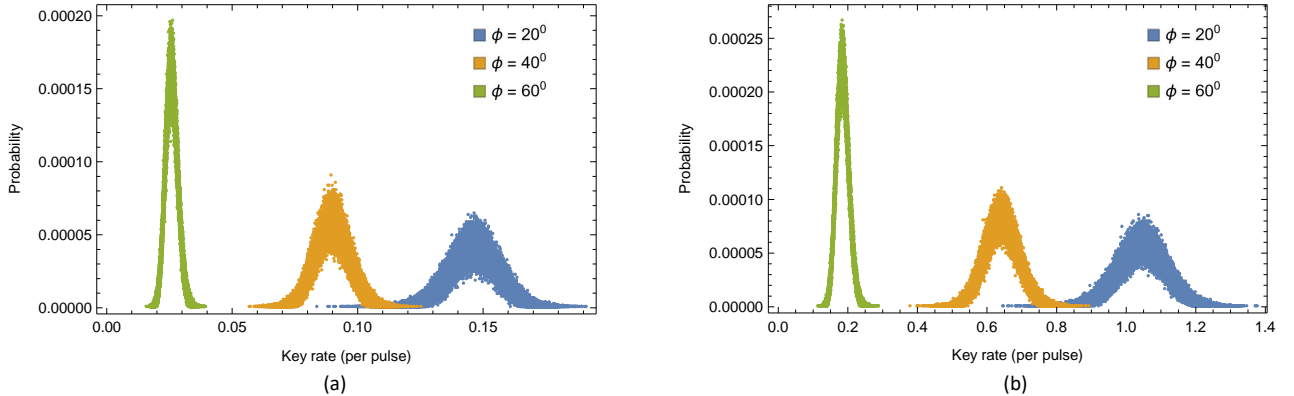


Figure 7. (Color online) Plot of distribution of key-rate variation for different zenith angles (ϕ) considering minimal noise, characterized by the parameter $q \ll 1$, under condition Day-1 utilizing qudit of dimension 32: (a) Probability distribution of key-rate for HD-Ext-B92 protocol, (b) Probability distribution of key-rate for HD-BB84 protocol under down-link configuration.

IV. CONCLUSION

In this paper, we study two protocols for QKD in higher dimensions. We analyze the key rates of these two higher dimensional protocols in the context of satellite-based secure quantum communication. To analyze the effectiveness of these schemes for satellite-based quantum communication, we employ a robust method known as the elliptic beam

approximation [111]. By employing a generalized model using this approach, we assess the performance of the HD-Ext-B92 and HD-BB84 protocols. The key rate per pulse and QBER are plotted against the noise parameter. Notably, our findings reveal that, in higher dimensions, HD-BB84 outperforms HD-Ext-B92 in terms of both key rate and noise tolerance. However, HD-BB84 experiences a more pronounced saturation of QBER in high dimensions. We deduce the key rate of the HD-Ext-B92 scheme without introducing any additional free parameters, as opposed to the approach discussed in Ref. [110], and is elaborated in Appendix A. Our analysis comprehensively demonstrates the impact of link transmittance on the weighted sum of key rate under nominal noise levels for both the schemes (HD-Ext-B92 and HD-BB84) under up-link and down-link configurations. Moreover, we delve into the analysis of PDR across different values of noise parameter (at the zenith position) and zenith angle (with nominal noise). Remarkably, the PDR exhibits consistent shapes across all scenarios. It is noteworthy that the graphical points are denser for HD-BB84; as anticipated this is because the HD-BB84 protocol makes use of two complete bases. Additionally, the probability tends to be higher for lower key rate values compared to higher ones. It may be noted that we employ normal and uniform distributions to model beam parameters. Alternative distributions may be employed to account for specific altitudes and atmospheric conditions. Consequently, variations in key rate could differ in our analysis, contingent on the consideration of atmospheric effects. For greater accuracy and interest, utilizing empirical data to obtain these results is recommended.

Numerous theoretical studies have been focused on finding the analytical probability distribution that best aligns with the experimentally observed transmittance of optical links in free space. The prevalent distributions employed are the log-normal [164, 165], Gamma-Gamma [166], and Double Weibull [167] distributions. The choice among these distributions depends on factors like turbulence intensity, link distance, and the setup of the transmitting and receiving telescopes. Conversely, the methodology employed in this study takes a constructive approach, enabling the determination of the PDT based on beam characteristics and atmospheric conditions. Further, our work can be expanded by examining the performance of a cube-sat, such as utilizing data from an existing satellite with an appropriate payload (say, from the Chinese satellite *Micius*), while optimizing the source intensity. This optimization would lead to an enhancement in the system's key rate and the ability to achieve longer link lengths (even when tolerating higher zenith angles) [168, 169]. Analysis of finite key in any quantum communication scheme would be interesting. Especially consideration of such effects is important in the context of satellite-based quantum communication because the limited duration of the connection between the ground station and the satellite would always lead to a finite key. Thus, future work could involve directing attention towards finite key analysis in scenarios involving higher dimensions, as well as assessing key rate performance in relation to atmospheric transmittance for satellite-based links. In summary, our investigations into the performance of higher-dimensional QKD protocols over satellite-based systems may have a substantial impact on both theoretical and experimental aspects of satellite-based quantum communication. Thus, the present work definitely establishes the advantages of using higher dimensional states in satellite-based quantum communication; but there are challenges associated with the experimental generation and maintenance of the qudits. In the near future we would like to address this technical issue and also to find the optimal choice of dimension that can provide a desired key rate.

Acknowledgment:

Authors acknowledge support from the Indian Space Research Organisation (ISRO) project no: ISRO/RES/3/906/22-23.

AVAILABILITY OF DATA AND MATERIALS

No additional data is needed for this work.

COMPETING INTERESTS

The authors declare that they have no competing interests.

FUNDING

Indian Space Research Organisation (ISRO) project no: ISRO/RES/3/906/22-23.

AUTHORS' CONTRIBUTIONS

SB conceptualized the problem. AD performed most of the calculations. AP and M checked the results. AP, SB, and AD analyzed the results. AP and SB supervised the work and all the authors contributed in writing the paper.

-
- [1] R. L. Rivest, A. Shamir, and L. M. Adleman, *Cryptographic communications system and method* (1983), US Patent 4,405,829.
- [2] F. Xu, X. Ma, Q. Zhang, H.-K. Lo, and J.-W. Pan, *Reviews of Modern Physics* **92**, 025002 (2020).
- [3] C. H. Bennett and G. Brassard, *Quantum cryptography: Public-key distribution and coin tossing*, in *Proc. IEEE Int. Conf. on Computers, Systems, and Signal Processing (Bangalore, India, 1984)*, pp. 175-179. (1984).
- [4] A. K. Ekert, *Physical Review Letters* **67**, 661 (1991).
- [5] C. H. Bennett, *Physical Review Letters* **68**, 3121 (1992).
- [6] C. H. Bennett, G. Brassard, and N. D. Mermin, *Physical Review Letters* **68**, 557 (1992).
- [7] V. Scarani, A. Acin, G. Ribordy, and N. Gisin, *Physical Review Letters* **92**, 057901 (2004).
- [8] R. Chatterjee, K. Joarder, S. Chatterjee, B. C. Sanders, and U. Sinha, *Physical Review Applied* **14**, 024036 (2020).
- [9] A. Pathak, *Elements of quantum computation and quantum communication* (CRC Press Boca Raton, 2013).
- [10] A. Dutta and A. Pathak, arXiv preprint arXiv:2212.13089 (2022).
- [11] C. Panayi, M. Razavi, X. Ma, and N. Lütkenhaus, *New Journal of Physics* **16**, 043005 (2014).
- [12] R. Valivarthi, Q. Zhou, C. John, F. Marsili, V. B. Verma, M. D. Shaw, S. W. Nam, D. Oblak, and W. Tittel, *Quantum Science and Technology* **2**, 04LT01 (2017).
- [13] C.-H. Zhang, C.-M. Zhang, and Q. Wang, *Communications in Theoretical Physics* **70**, 331 (2018).
- [14] K. Horodecki and M. Stankiewicz, *New Journal of Physics* **22**, 023007 (2020).
- [15] T. Brougham and D. K. Oi, *New Journal of Physics* **24**, 075002 (2022).
- [16] A. Tajima, T. Kondoh, T. Ochi, M. Fujiwara, K. Yoshino, H. Iizuka, T. Sakamoto, A. Tomita, E. Shimamura, S. Asami, et al., *Quantum Science and Technology* **2**, 034003 (2017).
- [17] A. Dutta and A. Pathak, *Quantum Information Processing* **22**, 13 (2023).
- [18] A. Dutta and A. Pathak, arXiv preprint arXiv:2308.05470 (2023).
- [19] D. A. Vajner, L. Rickert, T. Gao, K. Kaymazlar, and T. Heindel, *Advanced Quantum Technologies* **5**, 2100116 (2022).
- [20] T. K. Paraíso, R. I. Woodward, D. G. Marangon, V. Lovic, Z. Yuan, and A. J. Shields, *Advanced Quantum Technologies* **4**, 2100062 (2021).
- [21] H. P. Paudel, S. E. Crawford, Y.-L. Lee, R. A. Shugayev, M. N. Leuenberger, M. Syamlal, P. R. Ohodnicki, P. Lu, D. Mollot, and Y. Duan, *Advanced Quantum Technologies* **6**, 2300096 (2023).
- [22] T. Inagaki, N. Matsuda, O. Tadanaga, M. Asobe, and H. Takesue, *Optics Express* **21**, 23241 (2013).
- [23] B. Korzh, C. C. W. Lim, R. Houlmann, N. Gisin, M. J. Li, D. Nolan, B. Sanguinetti, R. Thew, and H. Zbinden, *Nature Photonics* **9**, 163 (2015).
- [24] S. Wengerowsky, S. K. Joshi, F. Steinlechner, J. R. Zichi, B. Liu, T. Scheidl, S. M. Dobrovolskiy, R. v. d. Molen, J. W. Los, V. Zwiller, et al., *npj Quantum Information* **6**, 5 (2020).
- [25] V. Scarani, H. Bechmann-Pasquinucci, N. J. Cerf, M. Dušek, N. Lütkenhaus, and M. Peev, *Reviews of Modern Physics* **81**, 1301 (2009).
- [26] H.-J. Briegel, W. Dür, J. I. Cirac, and P. Zoller, *Physical Review Letters* **81**, 5932 (1998).
- [27] N. Sangouard, C. Simon, H. De Riedmatten, and N. Gisin, *Reviews of Modern Physics* **83**, 33 (2011).
- [28] S. Pirandola, R. Laurenza, C. Ottaviani, and L. Banchi, *Nature communications* **8**, 15043 (2017).
- [29] M. Lucamarini, Z. L. Yuan, J. F. Dynes, and A. J. Shields, *Nature* **557**, 400 (2018).
- [30] Y.-M. Xie, C.-X. Weng, Y.-S. Lu, Y. Fu, Y. Wang, H.-L. Yin, and Z.-B. Chen, *Physical Review A* **107**, 042603 (2023).
- [31] Y.-M. Xie, Y.-S. Lu, C.-X. Weng, X.-Y. Cao, Z.-Y. Jia, Y. Bao, Y. Wang, Y. Fu, H.-L. Yin, and Z.-B. Chen, *PRX Quantum* **3**, 020315 (2022).
- [32] P. Zeng, H. Zhou, W. Wu, and X. Ma, *Nature Communications* **13**, 3903 (2022).
- [33] Y.-M. Xie, J.-L. Bai, Y.-S. Lu, C.-X. Weng, H.-L. Yin, and Z.-B. Chen, *Physical Review Applied* **19**, 054070 (2023).
- [34] J.-P. Chen, C. Zhang, Y. Liu, C. Jiang, W.-J. Zhang, Z.-Y. Han, S.-Z. Ma, X.-L. Hu, Y.-H. Li, H. Liu, et al., *Nature Photonics* **15**, 570 (2021).
- [35] L. Zhou, J. Lin, Y.-M. Xie, Y.-S. Lu, Y. Jing, H.-L. Yin, and Z. Yuan, *Physical Review Letters* **130**, 250801 (2023).
- [36] H.-T. Zhu, Y. Huang, H. Liu, P. Zeng, M. Zou, Y. Dai, S. Tang, H. Li, L. You, Z. Wang, et al., *Physical Review Letters* **130**, 030801 (2023).
- [37] Y. Liu, W.-J. Zhang, C. Jiang, J.-P. Chen, C. Zhang, W.-X. Pan, D. Ma, H. Dong, J.-M. Xiong, C.-J. Zhang, et al., *Physical Review Letters* **130**, 210801 (2023).
- [38] G. D. VanWiggeren and R. Roy, *Applied Optics* **38**, 3888 (1999).
- [39] J. Gordon and H. Kogelnik, *Proceedings of the National Academy of Sciences* **97**, 4541 (2000).
- [40] M. Toyoshima, H. Takenaka, Y. Shoji, Y. Takayama, M. Takeoka, M. Fujiwara, M. Sasaki, et al., *International Journal of Optics* **2011** (2011).
- [41] R. Bedington, J. M. Arrazola, and A. Ling, *npj Quantum Information* **3**, 30 (2017).

- [42] N. Ahmadi, S. Schwertfeger, P. Werner, L. Wiese, J. Lester, E. Da Ros, J. Krause, S. Ritter, M. Abasifard, C. Cholsuk, et al., *Advanced Quantum Technologies* p. 2300343 (2023).
- [43] R. Ursin, T. Jennewein, J. Kofler, J. M. Perdigue, L. Cacciapuoti, C. J. de Matos, M. Aspelmeyer, A. Valencia, T. Scheidl, A. Acin, et al., *Europhysics News* **40**, 26 (2009).
- [44] T. Scheidl, E. Wille, and R. Ursin, *New Journal of Physics* **15**, 043008 (2013).
- [45] V. Sharma and S. Banerjee, *Quantum Information Processing* **18**, 67 (2019).
- [46] O. Korotkova, M. Salem, A. Dogariu, and E. Wolf, *Waves in Random and Complex Media* **15**, 353 (2005).
- [47] J. Zhang, S. Ding, and A. Dang, *Applied Optics* **56**, 5145 (2017).
- [48] Z. Zhu, M. Janasik, A. Fyffe, D. Hay, Y. Zhou, B. Kantor, T. Winder, R. W. Boyd, G. Leuchs, and Z. Shi, *Nature Communications* **12**, 1666 (2021).
- [49] S. Pirandola, *Physical Review Research* **3**, 013279 (2021).
- [50] S. Pirandola, *Physical Review Research* **3**, 023130 (2021).
- [51] G. Xavier, N. Walenta, G. V. De Faria, G. Temporão, N. Gisin, H. Zbinden, and J. Von der Weid, *New Journal of Physics* **11**, 045015 (2009).
- [52] Y.-Y. Ding, W. Chen, H. Chen, C. Wang, S. Wang, Z.-Q. Yin, G.-C. Guo, Z.-F. Han, et al., *Optics Letters* **42**, 1023 (2017).
- [53] D.-D. Li, S. Gao, G.-C. Li, L. Xue, L.-W. Wang, C.-B. Lu, Y. Xiang, Z.-Y. Zhao, L.-C. Yan, Z.-Y. Chen, et al., *Optics Express* **26**, 22793 (2018).
- [54] S. P. Neumann, A. Buchner, L. Bulla, M. Bohmann, and R. Ursin, *Nature Communications* **13**, 6134 (2022).
- [55] Y. S. Lee, K. Mohammadi, L. Babcock, B. L. Higgins, H. Podmore, and T. Jennewein, *Review of Scientific Instruments* **93** (2022).
- [56] S. Chatterjee, K. Goswami, R. Chatterjee, and U. Sinha, *Communications Physics* **6**, 116 (2023).
- [57] D. Rideout, T. Jennewein, G. Amelino-Camelia, T. F. Demarie, B. L. Higgins, A. Kempf, A. Kent, R. Laflamme, X. Ma, R. B. Mann, et al., *Classical and Quantum Gravity* **29**, 224011 (2012).
- [58] S. K. Joshi, J. Pienaar, T. C. Ralph, L. Cacciapuoti, W. McCutcheon, J. Rarity, D. Giggenbach, J. G. Lim, V. Makarov, I. Fuentes, et al., *New Journal of Physics* **20**, 063016 (2018).
- [59] V. Giovannetti, S. Lloyd, and L. Maccone, *Nature* **412**, 417 (2001).
- [60] V. Giovannetti, S. Lloyd, L. Maccone, and F. Wong, *Physical Review Letters* **87**, 117902 (2001).
- [61] C. Ho, A. Lamas-Linares, and C. Kurtsiefer, *New Journal of Physics* **11**, 045011 (2009).
- [62] M. Ahmadi, D. E. Bruschi, C. Sabín, G. Adesso, and I. Fuentes, *Scientific Reports* **4**, 4996 (2014).
- [63] R. Ursin, F. Tiefenbacher, T. Schmitt-Manderbach, H. Weier, T. Scheidl, M. Lindenthal, B. Blauensteiner, T. Jennewein, J. Perdigue, P. Trojek, et al., *Nature Physics* **3**, 481 (2007).
- [64] P. Villoresi, T. Jennewein, F. Tamburini, M. Aspelmeyer, C. Bonato, R. Ursin, C. Pernechele, V. Luceri, G. Bianco, A. Zeilinger, et al., *New Journal of Physics* **10**, 033038 (2008).
- [65] A. Fedrizzi, R. Ursin, T. Herbst, M. Nespoli, R. Prevedel, T. Scheidl, F. Tiefenbacher, T. Jennewein, and A. Zeilinger, *Nature Physics* **5**, 389 (2009).
- [66] J. Yin, J.-G. Ren, H. Lu, Y. Cao, H.-L. Yong, Y.-P. Wu, C. Liu, S.-K. Liao, F. Zhou, Y. Jiang, et al., *Nature* **488**, 185 (2012).
- [67] J.-Y. Wang, B. Yang, S.-K. Liao, L. Zhang, Q. Shen, X.-F. Hu, J.-C. Wu, S.-J. Yang, H. Jiang, Y.-L. Tang, et al., *Nature Photonics* **7**, 387 (2013).
- [68] S. Nauerth, F. Moll, M. Rau, C. Fuchs, J. Horwath, S. Frick, and H. Weinfurter, *Nature Photonics* **7**, 382 (2013).
- [69] Y. Cao, H. Liang, J. Yin, H.-L. Yong, F. Zhou, Y.-P. Wu, J.-G. Ren, Y.-H. Li, G.-S. Pan, T. Yang, et al., *Optics Express* **21**, 27260 (2013).
- [70] C. J. Pugh, S. Kaiser, J.-P. Bourgoin, J. Jin, N. Sultana, S. Agne, E. Anisimova, V. Makarov, E. Choi, B. L. Higgins, et al., *Quantum Science and Technology* **2**, 024009 (2017).
- [71] C. Bonato, A. Tomaello, V. Da Deppo, G. Naletto, and P. Villoresi, *New Journal of Physics* **11**, 045017 (2009).
- [72] P. V. Trinh, A. Carrasco-Casado, H. Takenaka, M. Fujiwara, M. Kitamura, M. Sasaki, and M. Toyoshima, *Communications Physics* **5**, 225 (2022).
- [73] D. Vasylyev, W. Vogel, and F. Moll, *Physical Review A* **99**, 053830 (2019).
- [74] J.-P. Bourgoin, B. L. Higgins, N. Gigov, C. Holloway, C. J. Pugh, S. Kaiser, M. Cranmer, and T. Jennewein, *Optics Express* **23**, 33437 (2015).
- [75] H.-Y. Liu, X.-H. Tian, C. Gu, P. Fan, X. Ni, R. Yang, J.-N. Zhang, M. Hu, J. Guo, X. Cao, et al., *National Science Review* **7**, 921 (2020).
- [76] T. Jennewein and B. Higgins, *Physics World* **26**, 52 (2013).
- [77] I. Khan, B. Heim, A. Neuzner, and C. Marquardt, *Optics and Photonics News* **29**, 26 (2018).
- [78] J. Yin, Y. Cao, Y.-H. Li, S.-K. Liao, L. Zhang, J.-G. Ren, W.-Q. Cai, W.-Y. Liu, B. Li, H. Dai, et al., *Science* **356**, 1140 (2017).
- [79] S.-K. Liao, W.-Q. Cai, W.-Y. Liu, L. Zhang, Y. Li, J.-G. Ren, J. Yin, Q. Shen, Y. Cao, Z.-P. Li, et al., *Nature* **549**, 43 (2017).
- [80] H. Takenaka, A. Carrasco-Casado, M. Fujiwara, M. Kitamura, M. Sasaki, and M. Toyoshima, *Nature Photonics* **11**, 502 (2017).
- [81] S.-K. Liao, J. Lin, J.-G. Ren, W.-Y. Liu, J. Qiang, J. Yin, Y. Li, Q. Shen, L. Zhang, X.-F. Liang, et al., *Chinese Physics Letters* **34**, 090302 (2017).

- [82] J. Yin, Y.-H. Li, S.-K. Liao, M. Yang, Y. Cao, L. Zhang, J.-G. Ren, W.-Q. Cai, W.-Y. Liu, S.-L. Li, et al., *Nature* **582**, 501 (2020).
- [83] J. Yin, Y. Cao, Y.-H. Li, J.-G. Ren, S.-K. Liao, L. Zhang, W.-Q. Cai, W.-Y. Liu, B. Li, H. Dai, et al., *Physical Review Letters* **119**, 200501 (2017).
- [84] J.-G. Ren, P. Xu, H.-L. Yong, L. Zhang, S.-K. Liao, J. Yin, W.-Y. Liu, W.-Q. Cai, M. Yang, L. Li, et al., *Nature* **549**, 70 (2017).
- [85] S. Wehner, D. Elkouss, and R. Hanson, *Science* **362**, eaam9288 (2018).
- [86] H.-L. Yin, Y. Fu, C.-L. Li, C.-X. Weng, B.-H. Li, J. Gu, Y.-S. Lu, S. Huang, and Z.-B. Chen, *National Science Review* **10**, nwac228 (2023).
- [87] X.-Y. Cao, B.-H. Li, Y. Wang, Y. Fu, H.-L. Yin, and Z.-B. Chen, *Science Advances* **10**, eadk3258 (2024).
- [88] Z. Tang, R. Chandrasekara, Y. C. Tan, C. Cheng, L. Sha, G. C. Hiang, D. K. Oi, and A. Ling, *Physical Review Applied* **5**, 054022 (2016).
- [89] Z. Tang, R. Chandrasekara, Y. C. Tan, C. Cheng, K. Durak, and A. Ling, *Scientific Reports* **6**, 25603 (2016).
- [90] F. Steinlechner, O. de Vries, N. Fleischmann, E. Wille, E. Beckert, and R. Ursin, in *2016 Conference on Lasers and Electro-Optics (CLEO) (IEEE, 2016)*, pp. 1–2.
- [91] C.-Z. Peng, T. Yang, X.-H. Bao, J. Zhang, X.-M. Jin, F.-Y. Feng, B. Yang, J. Yang, J. Yin, Q. Zhang, et al., *Physical Review Letters* **94**, 150501 (2005).
- [92] I. Marcikic, A. Lamas-Linares, and C. Kurtsiefer, *Applied Physics Letters* **89** (2006).
- [93] C. Erven, C. Couteau, R. Laffamme, and G. Weihs, *Optics Express* **16**, 16840 (2008).
- [94] T. Scheidl, R. Ursin, A. Fedrizzi, S. Ramelow, X.-S. Ma, T. Herbst, R. Prevedel, L. Ratschbacher, J. Kofler, T. Jennewein, et al., *New Journal of Physics* **11**, 085002 (2009).
- [95] S. Ecker, B. Liu, J. Handsteiner, M. Fink, D. Rauch, F. Steinlechner, T. Scheidl, A. Zeilinger, and R. Ursin, *npj Quantum Information* **7**, 5 (2021).
- [96] T. Schmitt-Manderbach, H. Weier, M. Fürst, R. Ursin, F. Tiefenbacher, T. Scheidl, J. Perdigues, Z. Sodnik, C. Kurtsiefer, J. G. Rarity, et al., *Physical Review Letters* **98**, 010504 (2007).
- [97] U. Dubey, P. Bhole, A. Dutta, D. P. Behera, V. Losu, G. S. D. Pandeeti, A. R. Metkar, A. Banerjee, and A. Pathak, *Physics Open* p. 100210 (2024).
- [98] S.-K. Liao, W.-Q. Cai, J. Handsteiner, B. Liu, J. Yin, L. Zhang, D. Rauch, M. Fink, J.-G. Ren, W.-Y. Liu, et al., *Physical Review Letters* **120**, 030501 (2018).
- [99] A. Shenoy-Hejamadi, A. Pathak, and S. Radhakrishna, *Quanta* **6**, 1 (2017).
- [100] S. Pirandola, U. L. Andersen, L. Banchi, M. Berta, D. Bunandar, R. Colbeck, D. Englund, T. Gehring, C. Lupo, C. Ottaviani, et al., *Advances in Optics and Photonics* **12**, 1012 (2020).
- [101] M. Lucamarini, G. Di Giuseppe, and K. Tamaki, *Physical Review A* **80**, 032327 (2009).
- [102] S. Zhou, J. Yuan, Z.-Y. Wang, K. Ling, P.-X. Fu, Y.-H. Fang, Y.-X. Wang, Z. Liu, K. Porfyrikis, G. A. D. Briggs, et al., *Angewandte Chemie International Edition* **61**, e202115263 (2022).
- [103] E. Meier, L. de Melo, H. Lamsal, T. Bersano, E. Segura Carrillo, A. Harter, S. Omanakuttan, A. Mitra, I. Deutsch, M. Boshier, et al., *Bulletin of the American Physical Society* (2023).
- [104] D. Cozzolino, B. Da Lio, D. Bacco, and L. K. Oxenløwe, *Advanced Quantum Technologies* **2**, 1900038 (2019).
- [105] P. Malpani, N. Alam, K. Thapliyal, A. Pathak, V. Narayanan, and S. Banerjee, *Annalen der Physik* **531**, 1800318 (2019).
- [106] H. Bechmann-Pasquinucci and W. Tittel, *Physical Review A* **61**, 062308 (2000).
- [107] L. Sheridan and V. Scarani, *Physical Review A* **82**, 030301 (2010).
- [108] C. Vlachou, W. Krawec, P. Mateus, N. Paunković, and A. Souto, *Quantum Information Processing* **17**, 1 (2018).
- [109] V. Sharma, K. Thapliyal, A. Pathak, and S. Banerjee, *Quantum Information Processing* **15**, 4681 (2016).
- [110] H. Iqbal and W. O. Krawec, *Quantum Information Processing* **20**, 344 (2021).
- [111] D. Vasylyev, A. Semenov, and W. Vogel, *Physical Review Letters* **117**, 090501 (2016).
- [112] D. Vasylyev, A. Semenov, W. Vogel, K. Günthner, A. Thurn, Ö. Bayraktar, and C. Marquardt, *Physical Review A* **96**, 043856 (2017).
- [113] C. Liorni, H. Kampermann, and D. Bruß, *New Journal of Physics* **21**, 093055 (2019).
- [114] J. Bourgoin, E. Meyer-Scott, B. L. Higgins, B. Helou, C. Erven, H. Huebel, B. Kumar, D. Hudson, I. D'Souza, R. Girard, et al., *New Journal of Physics* **15**, 023006 (2013).
- [115] K. Tamaki, M. Koashi, and N. Imoto, *Physical Review Letters* **90**, 167904 (2003).
- [116] R. Matsumoto, in *2013 IEEE International Symposium on Information Theory (IEEE, 2013)*, pp. 351–353.
- [117] O. Amer and W. O. Krawec, in *2020 IEEE International Symposium on Information Theory (ISIT) (IEEE, 2020)*, pp. 1944–1948.
- [118] X.-M. Hu, C. Zhang, B.-H. Liu, Y. Cai, X.-J. Ye, Y. Guo, W.-B. Xing, C.-X. Huang, Y.-F. Huang, C.-F. Li, et al., *Physical Review Letters* **125**, 230501 (2020).
- [119] D. Bouwmeester, J.-W. Pan, K. Mattle, M. Eibl, H. Weinfurter, and A. Zeilinger, *Nature* **390**, 575 (1997).
- [120] D. Fattal, E. Diamanti, K. Inoue, and Y. Yamamoto, *Physical Review Letters* **92**, 037904 (2004).
- [121] S. Olmschenk, D. Matsukevich, P. Maunz, D. Hayes, L.-M. Duan, and C. Monroe, *Science* **323**, 486 (2009).
- [122] A. Furusawa, J. L. Sørensen, S. L. Braunstein, C. A. Fuchs, H. J. Kimble, and E. S. Polzik, *science* **282**, 706 (1998).
- [123] H. Yonezawa, S. L. Braunstein, and A. Furusawa, *Physical Review Letters* **99**, 110503 (2007).
- [124] N. Lee, H. Benichi, Y. Takeno, S. Takeda, J. Webb, E. Huntington, and A. Furusawa, *Science* **332**, 330 (2011).
- [125] A. C. Dada, J. Leach, G. S. Buller, M. J. Padgett, and E. Andersson, *Nature Physics* **7**, 677 (2011).

- [126] A. Martin, T. Guerreiro, A. Tiranov, S. Designolle, F. Fröwis, N. Brunner, M. Huber, and N. Gisin, *Physical Review Letters* **118**, 110501 (2017).
- [127] M. Kues, C. Reimer, P. Roztock, L. R. Cortés, S. Sciara, B. Wetz, Y. Zhang, A. Cino, S. T. Chu, B. E. Little, et al., *Nature* **546**, 622 (2017).
- [128] X.-M. Hu, W.-B. Xing, B.-H. Liu, Y.-F. Huang, C.-F. Li, G.-C. Guo, P. Erker, and M. Huber, *Physical Review Letters* **125**, 090503 (2020).
- [129] N. H. Valencia, V. Srivastav, M. Pivoluska, M. Huber, N. Friis, W. McCutcheon, and M. Malik, *Quantum* **4**, 376 (2020).
- [130] C.-Y. Lu and J.-W. Pan, *Nature Nanotechnology* **16**, 1294 (2021).
- [131] S. Thomas and P. Senellart, *Nature Nanotechnology* **16**, 367 (2021).
- [132] W.-Y. Hwang, *Physical Review Letters* **91**, 057901 (2003).
- [133] H.-K. Lo, X. Ma, and K. Chen, *Physical Review Letters* **94**, 230504 (2005).
- [134] J. Zhou, D. Huang, and Y. Guo, *Physical Review A* **98**, 042303 (2018).
- [135] J. Zhou, L. Wu, Y. Feng, H. Li, J. Shi, and R. Shi, *Quantum Information Processing* **22**, 356 (2023).
- [136] C.-M. Chen, X. Deng, W. Gan, J. Chen, and S. H. Islam, *The Journal of Supercomputing* **77**, 9046 (2021).
- [137] B. Feng, C. Lv, J. Liu, and T. Zhang, in *Journal of Physics: Conference Series* (IOP Publishing, 2021), vol. 1757, p. 012111.
- [138] E. Bai, Y. Zhang, X. Jiang, Y. Wu, Z. Shi, X. Lin, and Z. Pei, in *2021 IEEE International Conference on Power Electronics, Computer Applications (ICPECA)* (IEEE, 2021), pp. 571–574.
- [139] P. Zhang and X. Mao, in *Journal of Physics: Conference Series* (IOP Publishing, 2020), vol. 1621, p. 012017.
- [140] I. Devetak and A. Winter, *Proceedings of The Royal Society A: Mathematical, Physical and Engineering Sciences* **461**, 207 (2005).
- [141] R. Renner, N. Gisin, and B. Kraus, *Physical Review A* **72**, 012332 (2005).
- [142] W. O. Krawec, arXiv preprint arXiv:1608.07728 (2016).
- [143] N. J. Cerf, M. Bourennane, A. Karlsson, and N. Gisin, *Physical Review Letters* **88**, 127902 (2002).
- [144] M. Berta, M. Christandl, R. Colbeck, J. M. Renes, and R. Renner, *Nature Physics* **6**, 659 (2010).
- [145] K. Kraus, *Physical Review D* **35**, 3070 (1987).
- [146] H. Maassen and J. B. Uffink, *Physical Review Letters* **60**, 1103 (1988).
- [147] M. Christandl, R. Renner, and A. Ekert, arXiv preprint quant-ph/0402131 (2004).
- [148] J. Capmany, A. Ortigosa-Blanch, J. Mora, A. Ruiz-Alba, W. Amaya, and A. Martinez, *IEEE Journal of Selected Topics in Quantum Electronics* **15**, 1607 (2009).
- [149] S. M. Barnett, B. Huttner, and S. J. Phoenix, *Journal of Modern Optics* **40**, 2501 (1993).
- [150] S. Watanabe, R. Matsumoto, and T. Uyematsu, *Physical Review A* **78**, 042316 (2008).
- [151] R. Matsumoto and S. Watanabe, *IEICE Transactions on Fundamentals of Electronics, Communications and Computer Sciences* **91**, 2870 (2008).
- [152] K. Tamaki, M. Curty, G. Kato, H.-K. Lo, and K. Azuma, *Physical Review A* **90**, 052314 (2014).
- [153] D. Y. Vasylyev, A. Semenov, and W. Vogel, *Physical Review Letters* **108**, 220501 (2012).
- [154] G. C. Valley, *Applied Optics* **19**, 574 (1980).
- [155] R. Hufnagel and N. Stanley, *JOSA* **54**, 52 (1964).
- [156] J. K. Lawson and C. J. Carrano, in *Atmospheric Optical Modeling, Measurement, and Simulation II* (SPIE, 2006), vol. 6303, pp. 38–49.
- [157] R. Frehlich, R. Sharman, F. Vandenberghe, W. Yu, Y. Liu, J. Knievel, and G. Jumper, *Journal of Applied Meteorology and Climatology* **49**, 1742 (2010).
- [158] C. Tomasi and T. Paccagnella, *Pure and Applied Geophysics* **127**, 93 (1988).
- [159] C. Tomasi, *Journal of Geophysical Research: Atmospheres* **89**, 2563 (1984).
- [160] S. Wang, P. Huang, T. Wang, and G. Zeng, *New Journal of Physics* **20**, 083037 (2018).
- [161] M. J. Vargas, P. M. Benítez, and F. S. Bajo, *European Journal of Physics* **21**, 245 (2000).
- [162] X. Ma, C.-H. F. Fung, and M. Razavi, *Physical Review A* **86**, 052305 (2012).
- [163] F. Xu, H. Xu, and H.-K. Lo, *Physical Review A* **89**, 052333 (2014).
- [164] E. Limpert, W. A. Stahel, and M. Abbt, *BioScience* **51**, 341 (2001).
- [165] A. Stassinakis, H. Nistazakis, K. Peppas, and G. Tombras, *Optics & Laser Technology* **54**, 329 (2013).
- [166] M. Al-Habash, L. C. Andrews, and R. L. Phillips, *Optical Engineering* **40**, 1554 (2001).
- [167] N. D. Chatzidiamantis, H. G. Sandalidis, G. K. Karagiannidis, S. A. Kotsopoulos, and M. Matthaiou, in *2010 17th International Conference on Telecommunications* (IEEE, 2010), pp. 487–492.
- [168] Q. Dong, G. Huang, W. Cui, and R. Jiao, *Quantum Science and Technology* **7**, 015014 (2022).
- [169] W. Liang and R. Jiao, *New Journal of Physics* **22**, 083074 (2020).
- [170] A. Dutta and A. Pathak, *Quantum Information Processing* **21**, 369 (2022).

APPENDIX A

We recap the security analysis proposed in Ref. [110] and show our important modification in the investigation of the minimum value key rate (per pulse) for HD-Ext-B92 protocol. We elaborate the theorem [142] which provides the

lower bound of the conditional von Neumann entropy of classical-quantum state ρ_{aE} in Hilbert space²⁰ $\mathcal{H}_a \otimes \mathcal{H}_E$.

Theorem Let \mathcal{H}_a and \mathcal{H}_E are finite-dimensional Hilbert space and consider the following state of Alice and Eve in the form of density matrix,

$$\rho_{aE} = \frac{1}{M} \left(|0\rangle\langle 0|_a \otimes \left[\sum_{x=1}^d |E_x^0\rangle\langle E_x^0| \right] + |1\rangle\langle 1|_a \otimes \left[\sum_{x=1}^d |E_x^1\rangle\langle E_x^1| \right] \right), \quad (10)$$

where $M(> 0)$ is normalization factor, d has finite value, and each state²¹ $|E_x^y\rangle \in \mathcal{H}_E$. Assuming $K_x^y = \langle E_x^y | E_x^y \rangle \geq 0$, then,

$$S(a|E)_{\rho_{aE}} \geq \sum_{x=1}^d \left(\frac{K_x^0 + K_x^1}{M} \right) S_x,$$

where

$$S_x = \begin{cases} h\left(\frac{K_x^0}{K_x^0 + K_x^1}\right) - h(\delta_x) & \text{if } K_x^0 \wedge K_x^1 \geq 0, \\ 0 & \text{otherwise,} \end{cases}$$

and

$$\delta_x = \frac{1}{2} + \frac{\sqrt{(K_x^0 - K_x^1)^2 + 4\text{Re}^2\langle E_x^0 | E_x^1 \rangle}}{2(K_x^0 + K_x^1)}.$$

This *Theorem* serves as the foundation for our analysis, facilitating the derivation of the key rate equation for the protocol discussed throughout the remainder of this appendix.

The action of Eve's unitary operation \mathcal{E}_{TE} on Alice's transmitted state $|\Upsilon\rangle_T$ and Eve's ancilla state $|\chi\rangle_E$ is described in the following,

$$\mathcal{E}_{TE}|\Upsilon\rangle_T \otimes |\chi\rangle_E = \sum_{c=1}^d |c, E_c^\Upsilon\rangle_{TE},$$

and

$$\begin{aligned} \mathcal{E}_{TE}|\psi\rangle_T \otimes |\chi\rangle_E &= \mathcal{E}_{TE} \frac{1}{\sqrt{2}} (|m\rangle + |n\rangle)_T \otimes |\chi\rangle_E \\ &= \frac{1}{\sqrt{2}} \sum_{c=1}^d |c\rangle_T \otimes |F_c\rangle_E, \end{aligned}$$

where $|F_c\rangle_E := |E_c^m\rangle_E + |E_c^n\rangle_E$, and E_c^Υ is an arbitrary state in Eve's ancillary basis when Alice's transmitted state before and after Eve's operation are $|\Upsilon\rangle_T$ and $|c\rangle_T$, respectively. As \mathcal{E}_{TE} is a unitary operation the relation holds as $\sum_{c=1}^d \langle E_c^\Upsilon | E_c^\Upsilon \rangle = 1$.

After Eve's unitary operation on the classical-quantum state, $\rho_{aT} = \frac{1}{2} (|0\rangle\langle 0|_a \otimes |m\rangle\langle m|_T + |1\rangle\langle 1|_a \otimes |\psi\rangle\langle \psi|_T)$ is as following,

$$\begin{aligned} \rho_{aTE} &= \mathcal{E}_{TE}(\rho_{aT}) \\ &= \frac{1}{2} \left[|0\rangle\langle 0|_a \otimes P \left(\sum_{c=1}^d |c, E_c^m\rangle_{TE} \right) + |1\rangle\langle 1|_a \otimes P \left(\frac{1}{\sqrt{2}} \sum_{c=1}^d |c, F_c\rangle_{TE} \right) \right], \end{aligned} \quad (11)$$

where $P(|v\rangle) = |v\rangle\langle v|$ is projection operator. After receiving the transmitted register T Bob will apply the measurement operators $M_0 = I_a \otimes (I - |\psi\rangle\langle \psi|)_T \otimes I_E$ and $M_1 = I_a \otimes (I - |m\rangle\langle m|)_T \otimes I_E$ on T . Using Eq. (11) we can write density state after Bob's operations,

²⁰ Alice's register and Eve's quantum memory are represented in Hilbert space \mathcal{H}_a and \mathcal{H}_E , respectively.

²¹ Eve's states are not necessarily normalized, nor orthogonal; it might be that $|E_x^y\rangle \equiv 0$ also.

$$\begin{aligned}
\rho_{aTE}^0 &= M_0 (\rho_{aTE}) M_0^\dagger \\
&= \frac{1}{2} \left[|0\rangle\langle 0| \otimes P \left\{ \sum_{c \neq m, c \neq n} |c, E_c^m\rangle + \frac{1}{2} |m, E_m^m - E_n^m\rangle - \frac{1}{2} |n, E_m^m - E_n^m\rangle \right\} \right. \\
&\quad \left. + |1\rangle\langle 1| \otimes P \left\{ \frac{1}{\sqrt{2}} \left(\sum_{c \neq m, c \neq n} |c, F_c\rangle + \frac{1}{2} |m, F_m - F_n\rangle - \frac{1}{2} |n, F_m - F_n\rangle \right) \right\} \right]_{aTE}, \tag{12}
\end{aligned}$$

and

$$\begin{aligned}
\rho_{aTE}^1 &= M_1 (\rho_{aTE}) M_1^\dagger \\
&= \frac{1}{2} \left[|0\rangle\langle 0| \otimes P \left(\sum_{c \neq m} |c, E_c^m\rangle \right) + |1\rangle\langle 1| \otimes P \left(\frac{1}{\sqrt{2}} \sum_{c \neq m} |c, F_c\rangle \right) \right]_{aTE}. \tag{13}
\end{aligned}$$

After Bob gets his outcomes Eqs. (12) and (13) may be traced out the transit register T and include Bob's classical register b to keep his measurement result. Now the Eqs. (12) and (13) can be written like,

$$\begin{aligned}
\rho_{aEb}^0 &= \frac{1}{2} \left[|0\rangle\langle 0|_a \otimes \left\{ \sum_{c \neq m, c \neq n} |E_c^m\rangle\langle E_c^m| + \frac{1}{2} |(E_m^m - E_n^m)\rangle\langle (E_m^m - E_n^m)| \right\}_E \otimes |0\rangle\langle 0|_b \right. \\
&\quad \left. + |1\rangle\langle 1|_a \otimes \frac{1}{2} \left\{ \sum_{c \neq m, c \neq n} |F_c\rangle\langle F_c| + \frac{1}{2} |(F_m - F_n)\rangle\langle (F_m - F_n)| \right\}_E \otimes |0\rangle\langle 0|_b \right], \tag{14}
\end{aligned}$$

and

$$\rho_{aEb}^1 = \frac{1}{2} \left[|0\rangle\langle 0|_a \otimes \sum_{c \neq m} |E_c^m\rangle\langle E_c^m| \otimes |1\rangle\langle 1|_b + |1\rangle\langle 1|_a \otimes \frac{1}{2} \sum_{c \neq m} |F_c\rangle\langle F_c| \otimes |1\rangle\langle 1|_b \right]. \tag{15}$$

Adding up Eqs. (14) and (15), the non-normalized density operator which represents in one key-bit generation round is,

$$\begin{aligned}
\rho_{aEb} &= \rho_{aEb}^1 + \rho_{aEb}^0 \\
&= \frac{1}{2} |0\rangle\langle 0|_a \otimes \left[\left\{ \sum_{c \neq m, c \neq n} |E_c^m\rangle\langle E_c^m| + \frac{1}{2} |(E_m^m - E_n^m)\rangle\langle (E_m^m - E_n^m)| \right\} \otimes |0\rangle\langle 0|_b + \sum_{c \neq m} |E_c^m\rangle\langle E_c^m| \otimes |1\rangle\langle 1|_b \right] \\
&\quad + \frac{1}{2} |1\rangle\langle 1|_a \otimes \left[\frac{1}{2} \left\{ \sum_{c \neq m, c \neq n} |F_c\rangle\langle F_c| + \frac{1}{2} |(F_m - F_n)\rangle\langle (F_m - F_n)| \right\} \otimes |0\rangle\langle 0|_b + \frac{1}{2} \sum_{c \neq m} |F_c\rangle\langle F_c| \otimes |1\rangle\langle 1|_b \right]. \tag{16}
\end{aligned}$$

For computing the conditional entropy $H(a|b)$, we will show how the Eq. (16) is utilized to get the statistics for all combinations of Alice's and Bob's sifted key. Now, trace out Bob's register from Eq. (16) to keep the composite state of Alice's register and Eve's memory which is important to calculate $S(a|E)$. The final expression of the required density matrix is,

$$\begin{aligned}
\rho_{aE} &= \frac{1}{M} \left[|0\rangle\langle 0|_a \otimes \left(\sum_{c \neq m, c \neq n} |E_c^m\rangle\langle E_c^m| + \frac{1}{4} |E_m^m\rangle\langle E_m^m| - \frac{1}{4} |E_m^m\rangle\langle E_n^m| - \frac{1}{4} |E_n^m\rangle\langle E_m^m| + \frac{3}{4} |E_n^m\rangle\langle E_n^m| \right) \right. \\
&\quad \left. + |1\rangle\langle 1|_a \otimes \left(\sum_{c \neq m, c \neq n} \frac{1}{2} |F_c\rangle\langle F_c| + \frac{1}{8} |F_m\rangle\langle F_m| - \frac{1}{8} |F_m\rangle\langle F_n| - \frac{1}{8} |F_n\rangle\langle F_m| + \frac{3}{8} |F_n\rangle\langle F_n| \right) \right]_E, \tag{17}
\end{aligned}$$

where M is the normalization factor that can be calculated as,

$$\begin{aligned}
M &= \sum_{c \neq m, c \neq n} \langle E_c^m | E_c^m \rangle + \frac{1}{2} \langle E_n^m | E_n^m \rangle + \frac{1}{4} \langle (E_m^m - E_n^m) | (E_m^m - E_n^m) \rangle \\
&\quad + \frac{1}{2} \sum_{c \neq m, c \neq n} \langle F_c | F_c \rangle + \frac{1}{4} \langle F_n | F_n \rangle + \frac{1}{8} \langle (F_m - F_n) | (F_m - F_n) \rangle.
\end{aligned}$$

We modify the derivation for $S(a|E)$ using ρ_{aE} in comparison with the seminal work [110]. In our modified calculation, we express the terms of ρ_{aE} in Eve's two bases states, i.e., $\{E_c^m\}$ and $\{F_c\}$ which correspond to the bit values (i.e., 0 and 1) in Alice's register²².

Applying this above *theorem* we calculate the conditional von Neumann entropy,

$$S(a|E) \geq \sum_{c \neq m, c \neq n} \left(\frac{K_c^0 + K_c^1}{M} \right) S_c + \left(\frac{K_m^0 + K_m^1}{M} \right) S_m + \left(\frac{K_n^0 + K_n^1}{M} \right) S_n, \quad (18)$$

where

$$\begin{aligned} K_c^0 &:= \langle E_c^m | E_c^m \rangle, & K_c^1 &:= \frac{1}{2} \langle F_c | F_c \rangle, \forall c \neq m, n \\ K_m^0 &:= \frac{1}{4} \langle E_m^m | E_m^m \rangle, & K_m^1 &:= \frac{1}{8} \langle F_m | F_m \rangle, \\ K_n^0 &:= \frac{3}{4} \langle E_n^m | E_n^m \rangle, & K_n^1 &:= \frac{3}{8} \langle F_n | F_n \rangle. \end{aligned}$$

And

$$\begin{aligned} S_c &= h \left(\frac{K_c^0}{K_c^0 + K_c^1} \right) - h \left(\frac{1}{2} + \frac{\sqrt{(K_c^0 - K_c^1)^2 + 4 \operatorname{Re}^2 \langle E_c^m | \frac{1}{\sqrt{2}} F_c \rangle}}{2(K_c^0 + K_c^1)} \right), \\ S_m &= h \left(\frac{K_m^0}{K_m^0 + K_m^1} \right) - h \left(\frac{1}{2} + \frac{\sqrt{(K_m^0 - K_m^1)^2 + 4 \operatorname{Re}^2 \langle \frac{1}{2} E_m^m | \frac{1}{2\sqrt{2}} F_m \rangle}}{2(K_m^0 + K_m^1)} \right), \\ S_n &= h \left(\frac{K_n^0}{K_n^0 + K_n^1} \right) - h \left(\frac{1}{2} + \frac{\sqrt{(K_n^0 - K_n^1)^2 + 4 \operatorname{Re}^2 \langle \frac{3}{4\sqrt{2}} E_n^m | F_n \rangle}}{2(K_n^0 + K_n^1)} \right). \end{aligned}$$

Here, we briefly describe the *parameter estimation* for the required statistics to get the values in the above equations. Let $p_{vc}(p_{v\psi})$ be the observable parameter when Bob's measurement outcome is $|c\rangle (|\psi\rangle)$ using the $Z(X)$ basis when Alice sends state²³ $|\psi\rangle$. We may write in the form of the observable parameters $K_c^0 = p_{mc}$, $K_c^1 = p_{\psi c}$, $K_m^0 = \frac{1}{4} p_{mm}$, $K_m^1 = \frac{1}{4} p_{\psi m}$, $K_n^0 = \frac{3}{4} p_{mn}$, and $K_n^1 = \frac{3}{4} p_{\psi n}$.

$$\begin{aligned} \operatorname{Re} \langle E_c^m | \frac{1}{\sqrt{2}} F_c \rangle &= \frac{1}{\sqrt{2}} \left(\frac{p_{mc}}{2} + p_{\psi c} - \frac{p_{nc}}{2} \right), \\ \operatorname{Re} \langle \frac{1}{2} E_m^m | \frac{1}{2\sqrt{2}} F_m \rangle &= \frac{1}{4\sqrt{2}} \left(\frac{p_{mm}}{2} + p_{\psi m} - \frac{p_{nm}}{2} \right), \\ \operatorname{Re} \langle \frac{3}{4\sqrt{2}} E_n^m | F_n \rangle &= \frac{3}{4\sqrt{2}} \left(\frac{p_{mn}}{2} + p_{\psi n} - \frac{p_{nn}}{2} \right). \end{aligned}$$

In our study, we take only the depolarizing channel to evaluate the satellite-based effect of the HD-Ext-B92 protocol. Suppose the depolarizing channel $\mathcal{D}_q(\rho)$ with parameter q acting on a density operator ρ on a Hilbert space of dimension d . $\mathcal{D}_q(\rho)$ acts as follows,

$$\mathcal{D}_q(\rho) = \left(1 - \frac{d}{d-1} q \right) \rho + \frac{q}{d-1} I.$$

In the above, we have already mentioned the required parameter to calculate the key rate in terms of observable statistics. The observable statistics may be written in the effect of depolarizing channel scenario,

$$\begin{aligned} p_{mm} &= p_{nn} = p_{\psi\psi} = 1 - q, \\ p_{mc} &= p_{nc} = p_{\psi c} = \frac{q}{d-1}, \\ p_{m\psi} &= p_{n\psi} = p_{\psi m} = p_{\psi n} = \frac{1}{2} \left(1 - \frac{qd}{d-1} \right) + \frac{q}{d-1}. \end{aligned}$$

²² The above *Theorem* allows our expression of Eq. (17) unlike the Eq. (5) in Ref. [110].

²³ Here, the generalized state is $|\psi\rangle \in \{|m\rangle, |n\rangle, |\psi\rangle\}$, these statistics ($p_{vc(\psi)}$) come from the rounds where Alice and Bob do the same or different basis measurement (see Table 1 in Ref. [110]).

The above analysis is sufficient to evaluate $S(a|E)$ using Eq. (18), and to get the key rate we need the value of $H(a|b)$ which is analyzed²⁴ in the following,

$$H(a|b) = H(p_{00}, p_{01}, p_{10}, p_{11}) - h(p_{00} + p_{10}). \quad (19)$$

To compute Eq. (19), Alice and Bob use classical sampling i.e., the values of observable probabilities under the simulated channel. Using Eq. (16) with normalization term M ,

$$\begin{aligned} p_{00} &= \frac{1}{2M} (1 - p_{m\psi}), \\ p_{01} &= \frac{1}{2M} (1 - p_{mm}), \\ p_{10} &= \frac{1}{2M} (1 - p_{\psi\psi}), \\ p_{11} &= \frac{1}{2M} (1 - p_{\psi i}). \end{aligned}$$

These are the needful analyses that we recap above for estimating the minimum value of the key rate in Eq. (1).

APPENDIX B

We may write the first and second moments of the beam parameters in Eq. (6) concerning the connection detailed in Eq. (7). The angle of orientation of the elliptical profile φ is presumed to have a uniform distribution within the interval $[0, \frac{\pi}{2}]$. The mean value and the variance in the centroid position of the beam, in the case of up-links, are consistent for both the x and y directions, and they are equal to²⁵,

$$\begin{aligned} \langle x_0 \rangle &= \langle y_0 \rangle = 0, \\ \langle x_0^2 \rangle &= \langle y_0^2 \rangle = 0.419 \sigma_R^2 \mathcal{W}_0^2 \Omega^{-\frac{7}{6}} \frac{h}{L}, \end{aligned}$$

in this context, the term "Rytov parameter" represents the quantity $\sigma_R = 1.23 C_n^2 k^{\frac{7}{6}} L^{\frac{11}{6}}$, while $\Omega = \frac{k \mathcal{W}_0^2}{2L}$ stands for the Fresnel number, k is the optical wave number. The selected reference frame is such that $\langle x_0 \rangle = \langle y_0 \rangle = 0$. The mean and (co) variance of \mathcal{W}_i^2 can be written as,

$$\begin{aligned} \langle \mathcal{W}_i^2 \rangle &= \frac{\mathcal{W}_0^2}{\Omega^2} \left(1 + \frac{\pi}{8} L n_0 \mathcal{W}_0^2 \frac{h}{L} + 2.6 \sigma_R^2 \Omega^{\frac{5}{6}} \frac{h}{L} \right), \\ \langle \Delta \mathcal{W}_i^2 \Delta \mathcal{W}_j^2 \rangle &= (2\delta_{ij} - 0.8) \frac{\mathcal{W}_0^4}{\Omega^{\frac{19}{6}}} \left(1 + \frac{\pi}{8} L n_0 \mathcal{W}_0^2 \frac{h}{L} \right) \sigma_R^2 \frac{h}{L}. \end{aligned}$$

The same type of expressions also applies to down-links when considering the position of the beam centroid,

$$\begin{aligned} \langle x_0 \rangle &= \langle y_0 \rangle = 0, \\ \langle x_0^2 \rangle &= \langle y_0^2 \rangle = \alpha L, \end{aligned}$$

additionally, for the semi-major and semi-minor axes of the elliptical beam profile,

$$\begin{aligned} \langle \mathcal{W}_i^2 \rangle &= \frac{\mathcal{W}_0^2}{\Omega^2} \left(1 + \frac{\pi}{24} L n_0 \mathcal{W}_0^2 \left(\frac{h}{L} \right)^3 + 1.6 \sigma_R^2 \Omega^{\frac{5}{6}} \left(\frac{h}{L} \right)^{\frac{8}{3}} \right), \\ \langle \Delta \mathcal{W}_i^2 \Delta \mathcal{W}_j^2 \rangle &= (2\delta_{ij} - 0.8) \frac{3}{8} \frac{\mathcal{W}_0^4}{\Omega^{\frac{19}{6}}} \left(1 + \frac{\pi}{24} L n_0 \mathcal{W}_0^2 \left(\frac{h}{L} \right)^3 \right) \sigma_R^2 \left(\frac{h}{L} \right)^{\frac{8}{3}}, \end{aligned}$$

here, $\alpha \approx 2 \mu\text{rad}$ refers to the angular pointing error. Subsequently, the understanding of the probability distribution concerning the elliptic beam parameters (Eq. (6)) is applied to calculate the PDT utilizing Eq. (8) and a process of random sampling which is mentioned in Section II B.

²⁴ Assuming p_{ij} is the joint probability when Alice's and Bob's raw bit are "i" and "j" given that not eliminating that iteration [170].

²⁵ See for details Appendix C in Ref. [112].